

# Astrocyte scar formation aids central nervous system axon regeneration

Mark A. Anderson<sup>1\*†</sup>, Joshua E. Burda<sup>1\*</sup>, Yilong Ren<sup>1†</sup>, Yan Ao<sup>1</sup>, Timothy M. O'Shea<sup>1</sup>, Riki Kawaguchi<sup>2</sup>, Giovanni Coppola<sup>2</sup>, Baljit S. Khakh<sup>3</sup>, Timothy J. Deming<sup>4</sup> & Michael V. Sofroniew<sup>1</sup>

**Transected axons fail to regrow in the mature central nervous system. Astrocytic scars are widely regarded as causal in this failure. Here, using three genetically targeted loss-of-function manipulations in adult mice, we show that preventing astrocyte scar formation, attenuating scar-forming astrocytes, or ablating chronic astrocytic scars all failed to result in spontaneous regrowth of transected corticospinal, sensory or serotonergic axons through severe spinal cord injury (SCI) lesions. By contrast, sustained local delivery via hydrogel depots of required axon-specific growth factors not present in SCI lesions, plus growth-activating priming injuries, stimulated robust, laminin-dependent sensory axon regrowth past scar-forming astrocytes and inhibitory molecules in SCI lesions. Preventing astrocytic scar formation significantly reduced this stimulated axon regrowth. RNA sequencing revealed that astrocytes and non-astrocyte cells in SCI lesions express multiple axon-growth-supporting molecules. Our findings show that contrary to the prevailing dogma, astrocyte scar formation aids rather than prevents central nervous system axon regeneration.**

Transected axons fail to regrow spontaneously across severe tissue lesions in the mature mammalian central nervous system (CNS). Potential mechanisms include: (i) reduced intrinsic growth capacity of mature CNS neurons<sup>1–3</sup>; (ii) absence of external growth stimulating and supporting factors<sup>1,4,5</sup>; and (iii) presence of external inhibitory factors associated with myelin<sup>6,7</sup>, fibrotic tissue<sup>8</sup> or astrocytic scars<sup>9</sup>. Alleviating cellular and molecular mechanisms underlying axon regeneration failure is fundamental to improving CNS repair after traumatic injury, stroke or degenerative disease.

Astrocytic scars have been regarded as barriers to CNS axon regrowth since the mid-twentieth century on the basis of their appearance and early reports that attenuating astrocytic scar formation enabled spontaneous axon regrowth<sup>10,11</sup>. Although axon-growth-promoting effects of early scar attenuators proved illusory, reports correlating failed axon regrowth with presence of mature astrocytes<sup>12</sup> or astrocytic scars<sup>9</sup>, plus evidence that astrocytes produce chondroitin sulfate proteoglycans (CSPGs) that inhibit axon growth *in vitro*<sup>9</sup>, led to the widespread view that astrocytic scars are critical inhibitors of CNS axons and that nullifying this inhibition will lead to spontaneous axon regeneration.

Here we tested the hypothesis that astrocytic scar formation plays a causal role in the failure of transected mature CNS axons to regenerate across severe tissue lesions. We used multiple transgenic loss-of-function strategies to ablate scar-forming astrocytes, genetically attenuate scar-forming astrocytes or to ablate chronic astrocytic scars after severe SCI in adult mice. We quantified the effects of these manipulations on (i) spontaneous regeneration of three major types of CNS axons; (ii) total CSPG levels; (iii) genome-wide expression by astrocytes and non-astrocytes in SCI lesions of molecules associated with axon growth; and (iv) axon regeneration stimulated by conditioning lesions plus delivery via synthetic hydrogel depots of known axon-required growth factors missing from SCI lesions.

## No axon regrowth after preventing scars

We first determined effects of preventing astrocytic scar formation on the potential for spontaneous unstimulated axon regeneration through severe CNS lesions. After focal traumatic tissue damage, CNS lesions comprise central areas of non-neural lesion core tissue surrounded by narrow astrocytic scar borders<sup>13,14</sup>. Astrocytic scar formation is complete by two weeks after adult murine SCI and is critically dependent on astrocyte proliferation and STAT3 signalling<sup>15–18</sup>. We prevented astrocyte scar formation with two loss-of-function transgenic mouse models that either selectively kill proliferating scar-forming astrocytes<sup>15,16</sup> or delete STAT3 signalling selectively from astrocytes<sup>17,18</sup>, referred to respectively as TK+GCV or STAT3-CKO mice (Supplementary Information).

After severe crush SCI, wild-type mice formed dense astrocytic scars by two weeks that persisted for eight weeks, whereas TK+GCV and STAT3-CKO mice failed to form scars and instead exhibited larger areas of non-neural tissue around lesion centres that were essentially devoid of astrocytes from two to eight weeks after SCI (Fig. 1a–d, Extended Data Fig. 1 and Supplementary Information).

Effects of preventing astrocyte scar formation on axon regeneration were quantified in three axonal systems: (i) descending corticospinal tract (CST); (ii) ascending sensory tract (AST); and (iii) descending serotonergic (5HT) tract, visualized either by axonal tract tracing or immunohistochemistry (Fig. 1c, e–i and Supplementary Information). As expected after severe SCI in adult wild-type mice, transected CST and AST axons both exhibited moderate dieback away from lesion centres (Fig. 1c, e, g, h). Preventing astrocytic scar formation in either TK+GCV or STAT3-CKO mice failed to result in spontaneous regrowth of transected CST or AST axons through SCI lesions, and instead significantly increased axonal dieback (Fig. 1c, e, g, h). As expected<sup>19,20</sup>, transected 5HT axons exhibited little dieback from lesion centres (Fig. 1f, i). Preventing scar formation in TK+GCV or STAT3-CKO mice did not exacerbate dieback of 5HT axons.

<sup>1</sup>Department of Neurobiology, David Geffen School of Medicine, University of California, Los Angeles, California 90095-1763, USA. <sup>2</sup>Departments of Psychiatry and Neurology, David Geffen School of Medicine, University of California, Los Angeles, California 90095-1761, USA. <sup>3</sup>Department of Physiology, David Geffen School of Medicine, University of California, Los Angeles, California 90095-1751, USA. <sup>4</sup>Departments of Bioengineering, Chemistry and Biochemistry, University of California Los Angeles, Los Angeles, California 90095-1600, USA. <sup>†</sup>Present addresses: School of Life Sciences, Swiss Federal Institute of Technology (EPFL), SV BMI UPCourtine, Station 19, CH-1015 Lausanne, Switzerland (M.A.A.); Department of Spine Surgery, Tongji Hospital, Tongji University School of Medicine, Shanghai 200065, China (Y.R.).

\*These authors contributed equally to this work.

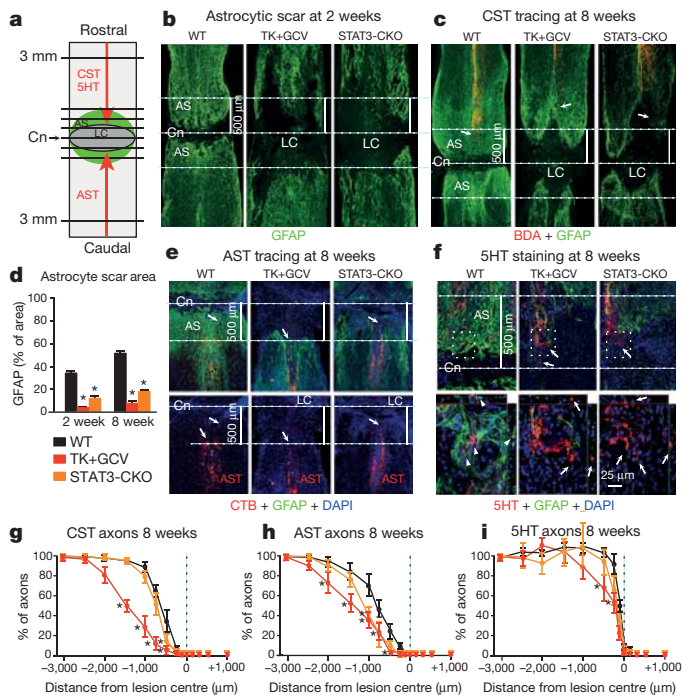


**Figure 1 | Preventing astrocytic scar formation does not lead to spontaneous regrowth of CST, AST or 5HT axons after SCI.**

**a**, Experiment summary schematic. Horizontal view of lesion core (LC) and astrocytic scar (AS) after SCI. Intercepts of CST, AST or 5HT axons with lines drawn at various distances from lesion centre (Cn) were counted and expressed as a percentage of all axons 3 mm proximal. **b, c, e, f**, Dotted lines demarcate lesion centre and 500  $\mu$ m on either side. **b, d**, Area occupied by GFAP-positive scar-forming astrocytes within 500  $\mu$ m either side of the lesion centre at 2 or 8 weeks after SCI.  $n = 6$ . **c, e**, Arrows depict most-caudal CST axons (biotinylated dextran amine tracing) or most-rostral AST axons (cholera toxin B tracing). **f**, Arrows in top images depict most caudally penetrating 5HT axons, boxed areas are shown below. In wild-type mice, 5HT axons are surrounded by the astrocytic scar (arrowheads). In TK+GCV and STAT3-CKO mice, many 5HT axons are not in contact with the astrocytic scar (arrows), but have not regrown. **g–i**, Numbers (means  $\pm$  s.e.m.) of CST (**g**), AST (**h**) and 5HT (**i**) axons at various distances from the SCI lesion centre as a percentage of the total number of axons present 3 mm proximal. CST,  $n = 6$  mice; AST and 5HT,  $n = 5$  mice;  $*P < 0.05$  versus wild type (ANOVA with Newman–Keuls).

Nevertheless, although many 5HT axons remained in lesion centres devoid of astrocytes, they also failed to regrow (Fig. 1f, i).

Thus, in spite of the essential absence of scar-forming astrocytes from SCI lesions for eight weeks after SCI in TK + GCV mice or STAT3-CKO mice, there was no spontaneous regeneration of transected CST, AST or 5HT axons through the lesions. This regrowth failure was particularly apparent for AST and 5HT axons, the axonal tips of which were often present along or within large areas devoid of astrocytes but did not regrow spontaneously through such areas (Fig. 1e, f).

### No axon regrowth after removing chronic scars

Acute astrocytic scar formation restricts inflammation and preserves neural tissue<sup>14–18</sup>. It has been proposed that after inflammation has resolved, chronic astrocytic scars are expendable and detrimental because they continually prevent axon regeneration. To test this hypothesis, we ablated chronic astrocytic scars five weeks after SCI with genetically targeted diphtheria toxin receptor and ultra-low doses of diphtheria toxin<sup>21</sup> (Fig. 2 and Supplementary Information). Distribution and specificity of targeting to mature astrocytic scars was verified with the genetic reporter tdTomato (Fig. 2b, Extended Data Fig. 1c and Supplementary Information). GFAP immunohistochemistry

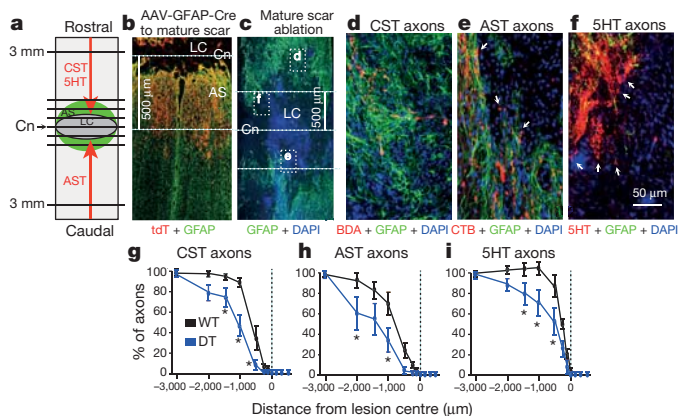


**Figure 2 | No spontaneous regrowth of CST, AST or 5HT axons after ablating chronic astrocytic scars.**

**a**, Experiment summary schematic. **b**, Selective targeting of tdTomato reporter to GFAP-positive scar-forming astrocytes in 500  $\mu$ m zone occupied by the astrocytic scar (see Extended Data Fig. 1c). **c**, Diphtheria toxin-mediated ablation of chronic astrocytic scar after severe SCI in mice with transgenically targeted diphtheria toxin receptor. Dotted lines indicate lesion centre (Cn) and 500  $\mu$ m on either side normally occupied by scar-forming astrocytes in wild-type (WT) mice. Boxes show locations of **d–f** in adjacent sections. **d**, CST axons are found only among GFAP-positive astrocytes proximal to ablated scar. **e**, AST axons are present at the margins of a large area depleted of scar but have not regrown (arrows). **f**, 5HT axons are present within an area depleted of scar but have not regrown (arrows). **g–i**, Numbers (means  $\pm$  s.e.m.) of CST (**g**), AST (**h**), or 5HT (**i**) axons at various distances from SCI lesion centres as a percentage of the total number of axons present at 3 mm proximal. CST,  $n = 6$  mice; AST and 5HT,  $n = 5$  mice;  $*P < 0.05$  versus wild type (ANOVA with Newman–Keuls).

verified efficient removal of chronic astrocytic scars (Fig. 2c). Axon quantitation ten weeks after SCI showed that transected CST, AST or 5HT axons all failed to regrow spontaneously through areas depleted of chronic astrocytic scars (Fig. 2d–i). Again, this failure was particularly notable for AST and 5HT axons in or along areas devoid of scar-forming astrocytes that did not regrow through these areas (Fig. 2e, f). We also ablated chronic astrocytic scars and adjacent astrocytes over larger areas to reach ‘died-back’ CST and AST axons, but this approach caused pronounced tissue degeneration and large lesions (Extended Data Fig. 1e) that contained essentially no detectable CST, AST or 5HT axons. These findings show that ablating chronic astrocytic scars fails to result in spontaneous regrowth of CST, AST or 5HT axons through SCI lesions, and that chronic astrocytic scars remain critical for sustaining tissue integrity.

### Multicellular CSPG production

We next looked for molecular mechanisms that might explain why ablating or attenuating astrocytic scars failed to enable spontaneous axon regrowth through severe lesions. CSPGs produced by astrocytic scars are regarded as the principal inhibitors of axon regeneration<sup>9</sup>. Total CSPG levels determined by dot blot with CS56 antibody<sup>9,22</sup> were, as expected<sup>9</sup>, significantly higher in our wild-type SCI lesions, but were not significantly reduced by transgenic ablation or disruption of astrocytic scar formation (Fig. 3a). Because diverse cells in SCI lesions including pericytes, fibroblast lineage cells and inflammatory cells<sup>13</sup> can produce CSPGs<sup>23</sup>, we examined cellular production of CSPG and GFAP and quantified immunohistochemically stained tissue areas. In SCI lesions of TK+GCV and STAT3-CKO mice, GFAP area was significantly reduced in both grey and white matter compared with wild type, whereas CSPG area was not significantly reduced in lesion core tissue or in regions of ablated astrocytic scars, which were filled with CSPG-positive, GFAP-negative cells (Figs 3b,c, Extended Data Fig. 2 and Supplementary Information). These findings show that non-astrocyte cells in SCI lesions produce substantive amounts of CSPGs



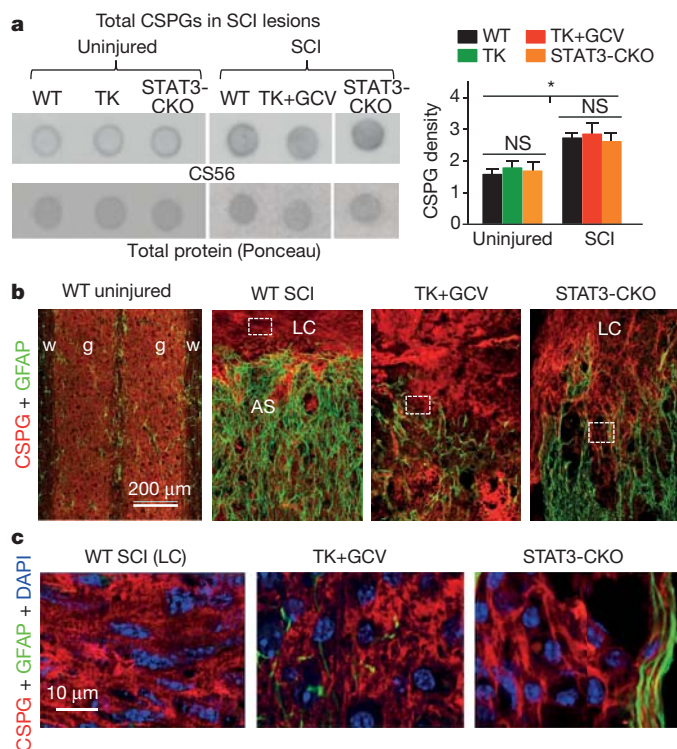


**Figure 3 | CSPG production by non-astrocyte cells in SCI lesions after ablation or attenuation of astrocytic scars.** **a**, Dot blots (left) and quantification (right, mean and s.e.m.) of total CSPGs detected by CS56 antibody relative to total protein levels (Ponceau).  $n = 4$  mice;  $*P < 0.05$  versus uninjured (ANOVA with Newman–Keuls). **b**, CS56 and GFAP immunohistochemistry (see Extended Data Fig. 2). AS, astrocytic scar; LC, lesion core; g, grey matter; w, white matter. **c**, Details of boxed areas in **b** showing CSPG production by GFAP-negative cells.

and that preventing astrocytic scar formation fails to reduce total CSPG production in SCI lesions.

### Genomic dissection of SCI lesions

Numerous molecules attract, repel, support or inhibit axon growth during development, and many of these are present in CNS lesions<sup>7,24,25</sup>. To look broadly at molecules produced by astrocytes or non-astrocyte cells in SCI lesions that might affect axon regrowth, we conducted genome-wide RNA sequencing of astrocyte-specific ribosome-associated RNA (ramRNA) precipitated via a haemagglutinin tag<sup>26</sup> transgenically targeted to either wild-type or STAT3-CKO astrocytes, and non-precipitated (flow-through) RNA deriving from non-astrocyte cells in the same tissue samples (Fig. 4, Extended Data Fig. 3 and Supplementary Information).

At two weeks after SCI, astrocytes and non-astrocyte cells in SCI lesions exhibited significantly altered expression of many genes in both wild-type and STAT3-CKO mice, and wild-type astrocytes exhibited expected known changes<sup>27</sup> (Extended Data Fig. 4a–d and Supplementary Information). Notably, 63% of genes significantly regulated by wild-type astrocytes were not significantly altered by STAT3-CKO astrocytes after SCI, and STAT3-CKO SCI astrocyte transcriptomes clustered more similarly towards uninjured astrocytes than towards wild-type SCI astrocytes (Fig. 4c, d).

We analysed 59 molecules reported to negatively or positively modulate axon growth in SCI lesions (Extended Data Table 1). In SCI lesions from wild-type mice, both astrocytes and non-astrocyte cells expressed a majority not only of 28 known axon inhibitors, including specific CSPGs, ephrins, netrins, neuropillins, plexins, slits and others, but also a majority of 31 known axon permissive molecules, including specific CSPGs, laminins, syndecans, glypicans, decorin and others (Fig. 4e). Notably, both astrocytes and non-astrocytes downregulated more axon

inhibitory molecules than were upregulated, and upregulated more than three times the number of axon-permissive molecules than were down-regulated. Preventing astrocytic scar formation in STAT3-CKO mice did not significantly decrease the expression by astrocytes or non-astrocytes of a single reported inhibitor, whereas eleven were upregulated, and significantly increased the expression of two permissive molecules, and decreased three, compared to wild-type SCI (Fig. 4e).

In agreement with our immunoblot and immunohistochemical CSPG findings (above), various individual CSPG ramRNAs were expressed by both astrocytes and non-astrocyte cells in SCI lesions (Fig. 4e). Interestingly, aggrecan, the prototypical CSPG used in axon growth inhibition studies *in vitro*<sup>28</sup>, was not detectably expressed by scar-forming astrocytes at either the ramRNA or immunohistochemistry of protein levels (Fig. 4e and Extended Data Fig. 5a). Other axon-inhibitory CSPGs, brevican, neurocan, versican and phosphacan, were all expressed by both scar-forming astrocytes and non-astrocyte cells in SCI lesions as revealed by RNA analysis (Fig. 4e) and confirmed by immunohistochemistry of protein for brevican and neurocan (Extended Data Figs 5b and 6a).

CSPGs are diverse with respect to inhibiting or supporting axon growth at both protein and sugar-epitope levels<sup>29,30</sup>. Of the five growth-inhibitory CSPGs, wild-type scar-forming astrocytes increased above normal only versican ramRNA, and significantly decreased neurocan and phosphacan (Fig. 4e). In contrast, ramRNAs of two axon-growth-supportive CSPGs, *Cspg4* (NG2) and *Cspg5* (neuroglycan C) (Extended Data Table 1), were significantly upregulated by scar-forming astrocytes (Fig. 4e) and both NG2 and CSPG5 clearly decorated scar-forming astrocytes, as revealed by immunohistochemistry (Extended Data Fig. 6b, c).

Our genomic findings show that: (i) STAT3-CKO prevents or attenuates a majority of genome-wide changes in astrocytes associated with astrogliosis and scar formation in wild-type mice; (ii) astrocytes and non-astrocyte cells in SCI lesions express a large, diverse mix of axon inhibitory and permissive molecules; (iii) non-astrocyte cells in SCI lesions substantively express CSPGs; (iv) preventing astrocyte scar formation with STAT3-CKO does not reduce expression of CSPGs or other inhibitory molecules in SCI lesions; (v) scar-forming astrocytes upregulate and substantively express axon-growth-supporting CSPGs, indicating that CS56 immune detection of total CSPG levels<sup>22</sup> need not indicate a purely axon-inhibitory environment; and (vi) scar-forming astrocytes and non-astrocyte cells in SCI lesions upregulate multiple axon-growth-permissive matrix molecules, including laminins.

### Axon regrowth in spite of scar formation

We next stimulated axon growth after SCI in the presence or absence of astrocytic scar formation. Developing axons do not grow by default but require stimulatory cues<sup>31</sup>. This requirement may apply also to regrowth of transected mature axons. Some transected mature AST axons can be stimulated to regrow in severe SCI lesions by activating neuron intrinsic growth programs with peripheral conditioning lesions<sup>32–34</sup>, and this regrowth can be significantly augmented by cell grafts that provide supportive matrix plus the neurotrophic factors NT3 and BDNF that attract AST axon growth during development<sup>35</sup>. We noted the essential absence of *Nt3* and *Bdnf* expression in our wild-type SCI lesions, combined with expression of permissive matrix molecules including laminins known to support developing AST axons<sup>36</sup> (Fig. 4e and Extended Data Table 1). We therefore tested effects of conditioning lesions plus local delivery of NT3 and BDNF on AST axon regeneration stimulated in the presence or absence of astrocyte scar formation (Fig. 5 and Extended Data Figs 7–9). Because cell grafts modify astrocytic scars<sup>35</sup> and provide permissive substrates for regrowing axons, we delivered NT3 and BDNF via synthetic hydrogel depots that do not modify astrocytic scar formation and provide prolonged neurotrophin delivery<sup>37–39</sup> (Fig. 5d; Supplementary Information).

No AST fibres regrew past astrocytic scars into lesion cores after SCI alone or with hydrogel without growth factors (Fig. 5a, j and

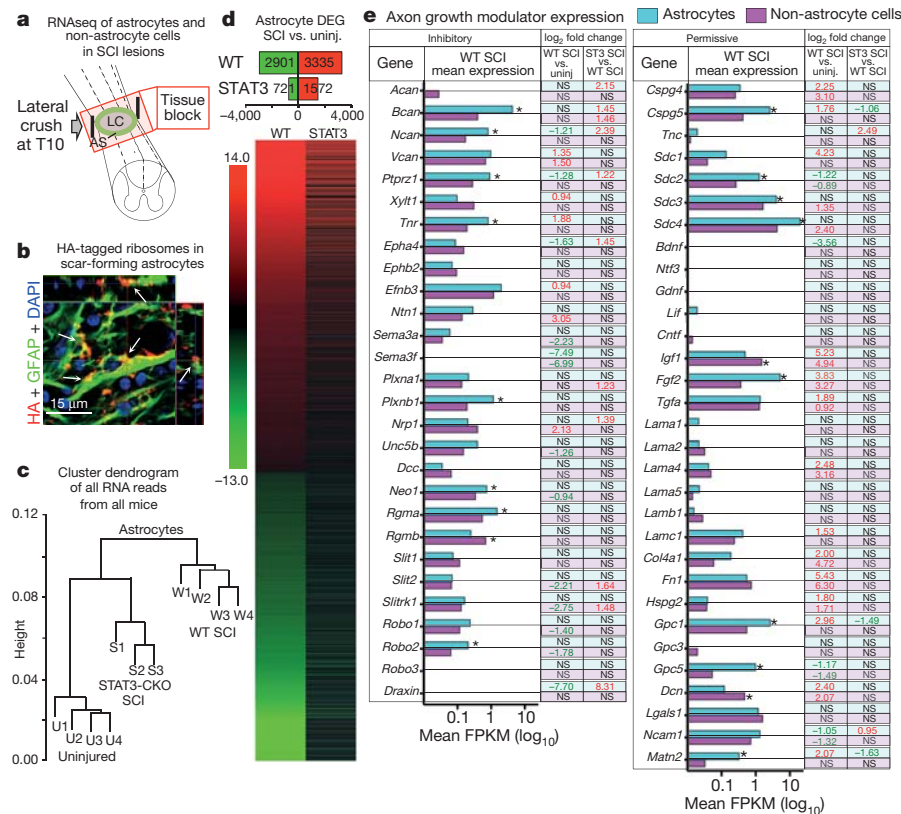


**Figure 4 | Genomic dissection of astrocytes and non-astrocyte cells in SCI lesions.** **a**, Schematic of tissue harvested for RNA sequencing (RNaseq). AS, astrocytic scar; LC, lesion core. **b**, Transgenically-targeted haemagglutinin (HA)-tagged ribosome clusters (arrows) among GFAP filaments in scar-forming astrocytes (see Extended Data Fig. 3a). **c**, Unsupervised hierarchical clustering dendrogram based on Pearson correlations shows that transcriptome profiles of STAT3-CKO SCI astrocytes cluster nearer to (and are more similar to) those of uninjured as compared to wild-type (WT) SCI astrocytes. **d**, Numbers and heat map of significantly differentially expressed genes (DEGs) in wild-type

Extended Data Fig. 7c). Small numbers of AST axons regrew into lesion cores in mice with SCI plus conditioning lesions alone, or SCI plus NT3 and BDNF without conditioning lesions (Fig. 5j, k and Extended Data Fig. 7c). By contrast, mice receiving both conditioning lesions plus NT3 and BDNF exhibited robust axon regrowth through and beyond astrocytic scars, and the number of axon intercepts counted at lesion centres averaged over 45% of that in intact sensory tracts 3 mm proximal to lesions (Fig. 5b, j, k and Extended Data Fig. 7c). Remarkably, these stimulated AST axons regrew profusely through, and past, dense astrocyte scars, and in spite of substantial CSPG (Fig. 5b, e–g, Extended Data Figs 7b, c and 8). AST axons stimulated to regrow in SCI lesions were thin and uniformly tracked along laminin surfaces, turning and even reversing direction along these surfaces as expected of regenerating axons<sup>40</sup>, whereas AST axons in intact gracile–cuneate tracts were coarsely beaded and were not in direct contact with laminin (Fig. 5h and Extended Data Fig. 9a–f). Hydrogel delivery of anti-CD29 laminin-integrin function-blocking antibodies<sup>36</sup> together with NT3 and BDNF significantly reduced AST axon regrowth in lesion cores by 73%, demonstrating that laminin interactions were critical for stimulated AST axon regrowth (Fig. 5i, j, Extended Data Fig. 9g–i and Supplementary Information). Lastly, preventing astrocyte scar formation did not augment AST axon regrowth stimulated by conditioning lesions plus NT3 and BDNF, but instead completely prevented, or significantly attenuated, axon regrowth in TK + GCV mice and STAT3-CKO mice, respectively (Fig. 5c, j, k), demonstrating that astrocytic scar formation aids, rather than inhibits appropriately stimulated AST axon regeneration after SCI.

astrocytes after SCI and the comparative differential expression profile of that specific cohort of genes in STAT3-CKO SCI astrocytes. Differential expression relative to uninjured, false discovery rate (FDR) < 0.1. **e**, Histogram of astrocyte and non-astrocyte expression of axon-growth-inhibitory or -permissive molecules after SCI shown as mean FPKM (fragments per kilobase of transcript sequence per million mapped fragments). Asterisks indicate significant differences between astrocytes and non-astrocytes, FDR < 0.1. Numbers show significant log<sub>2</sub> fold differences. Red, upregulated; green, downregulated; NS, non-significant; ST3 SCI, STAT3-CKO SCI.

## Discussion

Our findings show that contrary to prevailing dogma, astrocytic scar formation is not a principal cause for the failure of injured mature CNS axons to regrow across severe CNS lesions and that scar-forming astrocytes permit and support robust amounts of appropriately stimulated CNS axon regeneration. Although our observations with stimulated AST axon regeneration needs extension to other axonal systems, our findings are consistent with evidence that: (i) astrocytes can support growth of different CNS axons *in vivo* during development<sup>41,42</sup> or after mature CNS injury<sup>19,43</sup>; (ii) genetic activation of axonal growth programs by mature neurons leads to axon regeneration across CNS lesions only when scar-forming astrocyte bridges are present<sup>2,44</sup>; and (iii) grafts of progenitor-derived astrocytes support axon regeneration through non-neural SCI lesion cores<sup>45,46</sup>.

The predominant mechanistic proposal for astrocytic scar inhibition of axon regeneration is CSPG production<sup>9</sup>. However, specific CSPGs can support or repel axon growth (see Extended Data Table 1). We show that scar-forming astrocytes upregulate growth supportive CSPG4 and CSPG5, and that both astrocytes and non-astrocytes in SCI lesions express multiple axon-growth-supportive molecules, including laminins. Axon growth and guidance depend both on intrinsic growth potential<sup>2,3,31,32,47</sup> and on a balance of extrinsic regulatory cues that modulate one another's effects on growth cones<sup>25</sup>. Our findings show that sustained delivery of required axon-specific growth factors not adequately expressed in SCI lesions, combined with activation of neuron-intrinsic growth programs, can stimulate robust regrowth of transected axons along specifically required supportive matrix cues in



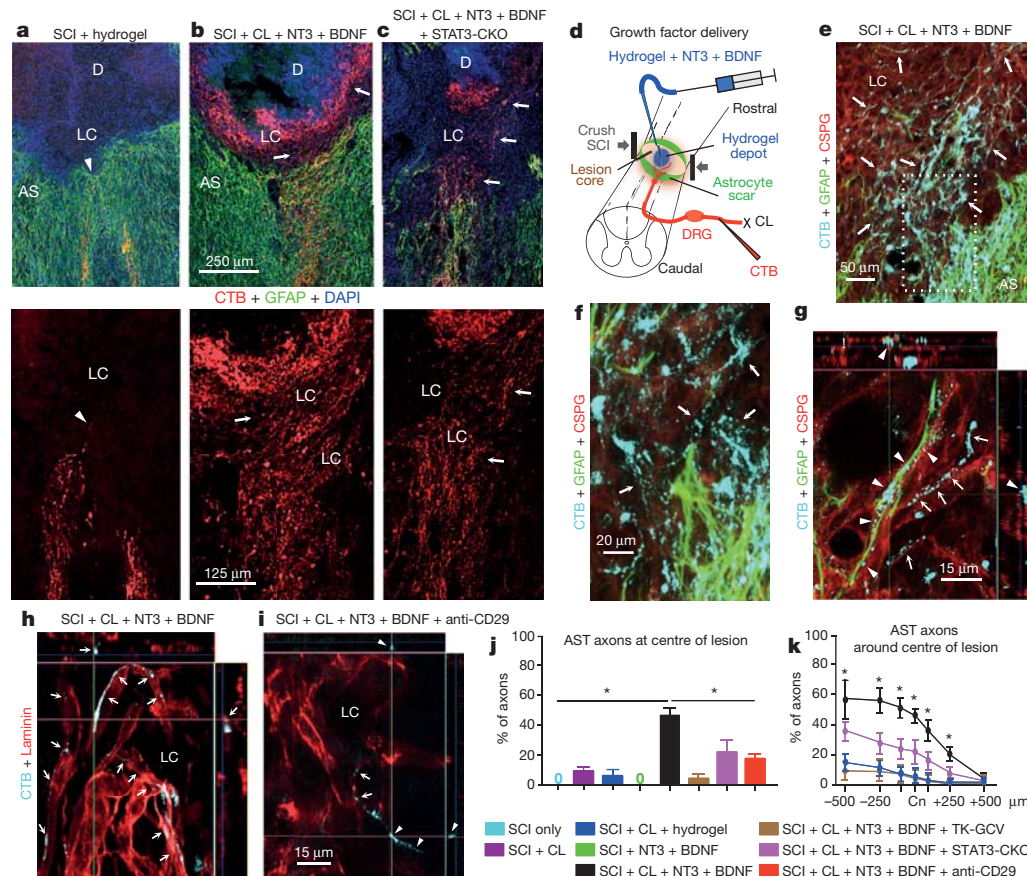


**Figure 5 | Robust regrowth of AST axons can be stimulated after wild-type SCI and is significantly attenuated by preventing astrocytic scar formation.** **a–c**, Top, AST axons (choleratoxin B tracing) plus GFAP immunohistochemistry. Bottom, AST axons alone. AS, astrocytic scar; D, hydrogel depot; LC, lesion core. **a**, Wild-type mouse, SCI and hydrogel only (no growth factors). Arrowhead denotes most rostrally penetrating axons that do not pass beyond AS. **b**, Wild-type mouse, SCI plus conditioning lesion (CL) and hydrogel depot (D) with NT3 + BDNF. Arrows denote robust regrowth of AST axons past the scar into the lesion core and along, but not into, the depot that releases NT3 + BDNF but that provides no adhesive matrix. **c**, STAT3-CKO mouse, SCI plus conditioning lesions and NT3 + BDNF depot. Arrows denote regrowth of AST axons into the lesion core. **d**, Experiment summary schematic. CTB, choleratoxin B; DRG, dorsal root ganglion. **e–g**, Wild-type mice, AST plus GFAP and

CSPG (CS56) immunohistochemistry. Box in **e** is shown in **f**, **e**, Arrows denote robust regrowth of stimulated AST axons past the astrocytic scar into the lesion core through CSPG. **g**, Regrowing AST axons track along CSPG-positive GFAP-negative structures (arrows) or along CSPG-positive GFAP-positive astrocyte processes (arrowheads) (see Extended Data Figs 7 and 8 for single channel images of **e–g**). **h**, **i**, AST axons plus laminin immunohistochemistry. **h**, **i**, Arrows indicate regrowing stimulated AST axons tracking along laminin. **i**, Arrowheads indicate stimulated AST axons exposed to anti-CD29 antibody and failing to maintain contact with laminin. **j**, **k**, Numbers of AST axons at SCI lesion centre (Cn) (**j**) or on either side (**k**) expressed as a percentage of all axons 3 mm proximal.  $n = 5$ ;  $*P < 0.05$  versus all other groups,  $\#P < 0.05$  versus all groups except STAT3-CKO (ANOVA with Newman–Keuls).

spite of the presence of inhibitory cues, and that this stimulated axon regrowth can occur either in direct contact with scar-forming astrocyte processes or independently of astrocyte processes. These observations provide direct evidence that the requirements for achieving axon regeneration across severe CNS lesions, where transected axons lack intrinsic and extrinsic conditions for long-distance regrowth, are fundamentally different from requirements to achieve local neurite outgrowth in intact but reactive perilesional grey matter, where conditions compatible with axon terminal growth and remodelling are present and where blocking inhibitory regulators such as CSPGs and others produced by astrocytes and other cells may be sufficient to promote axon sprouting that might also improve function<sup>9,15,24,28,40,48</sup>. Our findings have important implications for CNS repair strategies by demonstrating that rather than being hostile to axon growth, newly generated immature scar-forming astrocytes derived after SCI from endogenous progenitors<sup>18,41,44</sup>, and potentially from grafted progenitors<sup>45,46</sup>, aid axon regeneration and may represent exploitable bridges for regrowing axons across severe CNS lesions.

**Online Content** Methods, along with any additional Extended Data display items and Source Data, are available in the online version of the paper; references unique to these sections appear only in the online paper.

Received 23 October 2015; accepted 26 February 2016.

Published online 30 March 2016.

- Ramón y Cajal, S. *Degeneration and Regeneration of the Nervous System* (Oxford Univ. Press, 1928).
- Sun, F. *et al.* Sustained axon regeneration induced by co-deletion of PTEN and SOCS3. *Nature* **480**, 372–375 (2011).
- Liu, K., Tedeschi, A., Park, K. K. & He, Z. Neuronal intrinsic mechanisms of axon regeneration. *Annu. Rev. Neurosci.* **34**, 131–152 (2011).
- Richardson, P. M., McGuinness, U. M. & Aguayo, A. J. Axons from CNS neurons regenerate into PNS grafts. *Nature* **284**, 264–265 (1980).
- David, S. & Aguayo, A. J. Axonal elongation into peripheral nervous system “bridges” after central nervous system injury in adult rats. *Science* **214**, 931–933 (1981).
- Schwab, M. E. Functions of Nogo proteins and their receptors in the nervous system. *Nature Rev. Neurosci.* **11**, 799–811 (2010).
- Harel, N. Y. & Strittmatter, S. M. Can regenerating axons recapitulate developmental guidance during recovery from spinal cord injury? *Nature Rev. Neurosci.* **7**, 603–616 (2006).
- Klapka, N. & Müller, H. W. Collagen matrix in spinal cord injury. *J. Neurotrauma* **23**, 422–435 (2006).
- Silver, J. & Miller, J. H. Regeneration beyond the glial scar. *Nature Rev. Neurosci.* **5**, 146–156 (2004).
- Windle, W. F., Clemente, C. D. & Chambers, W. W. Inhibition of formation of a glial barrier as a means of permitting a peripheral nerve to grow into the brain. *J. Comp. Neurol.* **96**, 359–369 (1952).

11. Windle, W. F. Regeneration of axons in the vertebrate central nervous system. *Physiol. Rev.* **36**, 427–440 (1956).
12. Liuzzi, F. J. & Lasek, R. J. Astrocytes block axonal regeneration in mammals by activating the physiological stop pathway. *Science* **237**, 642–645 (1987).
13. Burda, J. E. & Sofroniew, M. V. Reactive gliosis and the multicellular response to CNS damage and disease. *Neuron* **81**, 229–248 (2014).
14. Sofroniew, M. V. Astrocyte barriers to neurotoxic inflammation. *Nature Rev. Neurosci.* **16**, 249–263 (2015).
15. Bush, T. G. *et al.* Leukocyte infiltration, neuronal degeneration and neurite outgrowth after ablation of scar-forming, reactive astrocytes in adult transgenic mice. *Neuron* **23**, 297–308 (1999).
16. Faulkner, J. R. *et al.* Reactive astrocytes protect tissue and preserve function after spinal cord injury. *J. Neurosci.* **24**, 2143–2155 (2004).
17. Herrmann, J. E. *et al.* STAT3 is a critical regulator of astrogliosis and scar formation after spinal cord injury. *J. Neurosci.* **28**, 7231–7243 (2008).
18. Wanner, I. B. *et al.* Glial scar borders are formed by newly proliferated, elongated astrocytes that interact to corral inflammatory and fibrotic cells via STAT3-dependent mechanisms after spinal cord injury. *J. Neurosci.* **33**, 12870–12886 (2013).
19. Lee, J. K. *et al.* Combined genetic attenuation of myelin and semaphorin-mediated growth inhibition is insufficient to promote serotonergic axon regeneration. *J. Neurosci.* **30**, 10899–10904 (2010).
20. Hawthorne, A. L. *et al.* The unusual response of serotonergic neurons after CNS injury: lack of axonal dieback and enhanced sprouting within the inhibitory environment of the glial scar. *J. Neurosci.* **31**, 5605–5616 (2011).
21. Buch, T. *et al.* A Cre-inducible diphtheria toxin receptor mediates cell lineage ablation after toxin administration. *Nature Methods* **2**, 419–426 (2005).
22. Avnur, Z. & Geiger, B. Immunocytochemical localization of native chondroitin-sulfate in tissues and cultured cells using specific monoclonal antibody. *Cell* **38**, 811–822 (1984).
23. Mikami, T. & Kitagawa, H. Biosynthesis and function of chondroitin sulfate. *Biochim. Biophys. Acta* **1830**, 4719–4733 (2013).
24. Mironova, Y. A. & Giger, R. J. Where no synapses go: gatekeepers of circuit remodeling and synaptic strength. *Trends Neurosci.* **36**, 363–373 (2013).
25. Lin, A. C. & Holt, C. E. Local translation and directional steering in axons. *EMBO J.* **26**, 3729–3736 (2007).
26. Sanz, E. *et al.* Cell-type-specific isolation of ribosome-associated mRNA from complex tissues. *Proc. Natl Acad. Sci. USA* **106**, 13939–13944 (2009).
27. Zamanian, J. L. *et al.* Genomic analysis of reactive astrogliosis. *J. Neurosci.* **32**, 6391–6410 (2012).
28. Lang, B. T. *et al.* Modulation of the proteoglycan receptor PTPsigma promotes recovery after spinal cord injury. *Nature* **518**, 404–408 (2015).
29. Yamaguchi, Y. Lecticans: organizers of the brain extracellular matrix. *Cell. Mol. Life Sci.* **57**, 276–289 (2000).
30. Miller, G. M. & Hsieh-Wilson, L. C. Sugar-dependent modulation of neuronal development, regeneration, and plasticity by chondroitin sulfate proteoglycans. *Exp. Neurol.* **274**, 115–125 (2015).
31. Goldberg, J. L. *et al.* Retinal ganglion cells do not extend axons by default: promotion by neurotrophic signaling and electrical activity. *Neuron* **33**, 689–702 (2002).
32. Richardson, P. M. & Issa, V. M. Peripheral injury enhances central regeneration of primary sensory neurones. *Nature* **309**, 791–793 (1984).
33. Neumann, S. & Woolf, C. J. Regeneration of dorsal column fibers into and beyond the lesion site following adult spinal cord injury. *Neuron* **23**, 83–91 (1999).
34. Omura, T. *et al.* Robust Axonal regeneration occurs in the injured CAST/Ei mouse CNS. *Neuron* **86**, 1215–1227 (2015).
35. Alto, L. T. *et al.* Chemotropic guidance facilitates axonal regeneration and synapse formation after spinal cord injury. *Nature Neurosci.* **12**, 1106–1113 (2009).
36. Plantman, S. *et al.* Integrin-laminin interactions controlling neurite outgrowth from adult DRG neurons *in vitro*. *Mol. Cell. Neurosci.* **39**, 50–62 (2008).
37. Nowak, A. P. *et al.* Rapidly recovering hydrogel scaffolds from self-assembling diblock copolypeptide amphiphiles. *Nature* **417**, 424–428 (2002).
38. Yang, C. Y. *et al.* Biocompatibility of amphiphilic diblock copolypeptide hydrogels in the central nervous system. *Biomaterials* **30**, 2881–2898 (2009).
39. Song, B. *et al.* Sustained local delivery of bioactive nerve growth factor in the central nervous system via tunable diblock copolypeptide hydrogel depots. *Biomaterials* **33**, 9105–9116 (2012).
40. Tuszynski, M. H. & Steward, O. Concepts and methods for the study of axonal regeneration in the CNS. *Neuron* **74**, 777–791 (2012).
41. Brosius Lutz, A. & Barres, B. A. Contrasting the glial response to axon injury in the central and peripheral nervous systems. *Dev. Cell* **28**, 7–17 (2014).
42. Mason, C. A., Edmondson, J. C. & Hatten, M. E. The extending astroglial process: development of glial cell shape, the growing tip, and interactions with neurons. *J. Neurosci.* **8**, 3124–3134 (1988).
43. Kawaja, M. D. & Gage, F. H. Reactive astrocytes are substrates for the growth of adult CNS axons in the presence of elevated levels of nerve growth factor. *Neuron* **7**, 1019–1030 (1991).
44. Zukor, K. *et al.* Short hairpin RNA against PTEN enhances regenerative growth of corticospinal tract axons after spinal cord injury. *J. Neurosci.* **33**, 15350–15361 (2013).
45. Shih, C. H., Lacagnina, M., Leuer-Biscioti, K. & Proschel, C. Astroglial-derived periostin promotes axonal regeneration after spinal cord injury. *J. Neurosci.* **34**, 2438–2443 (2014).
46. Zhang, S. *et al.* Thermoresponsive copolypeptide hydrogel vehicles for CNS cell delivery. *ACS Biomater. Sci. Eng.* **1**, 705–717 (2015).
47. Ruschel, J. *et al.* Systemic administration of epothilone B promotes axon regeneration after spinal cord injury. *Science* **348**, 347–352 (2015).
48. Cafferty, W. B., McGee, A. W. & Strittmatter, S. M. Axonal growth therapeutics: regeneration or sprouting or plasticity? *Trends Neurosci.* **31**, 215–220 (2008).

**Supplementary Information** is available in the online version of the paper.

**Acknowledgements** We thank D. W. Bergles for the NG2 antibody, and the Microscopy Core Resource of the UCLA Broad Stem Cell Research Center-CIRM Laboratory. This work was supported by the US National Institutes of Health (NS057624 and NS084030 to M.V.S.; P30 NS062691 to G.C. and NS060677, MH099559A, MH104069 to B.S.K.), and the Dr. Miriam and Sheldon G. Adelson Medical Foundation (M.V.S. and T.J.D.), and Wings for Life (M.V.S.).

**Author Contributions** M.A.A., J.E.B., B.S.K., T.J.D. and M.V.S. designed experiments; M.A.A., J.E.B., Y.R. and Y.A. conducted experiments; M.A.A., J.E.B., Y.A., T.M.O., R.K., G.C. and M.V.S. analysed data. M.A.A., J.E.B., T.M.O., B.S.K., T.J.D. and M.V.S. prepared the manuscript.

**Author Information** Raw and normalized genomic data have been deposited in the NCBI Gene Expression Omnibus and are accessible through accession number GSE76097 and via a searchable, open-access website <https://astrocyte.mseq.sofroniewlab.neurobio.ucla.edu>. Reprints and permissions information is available at [www.nature.com/reprints](http://www.nature.com/reprints). The authors declare no competing financial interests. Readers are welcome to comment on the online version of the paper. Correspondence and requests for materials should be addressed to M.V.S. ([sofroniew@mednet.ucla.edu](mailto:sofroniew@mednet.ucla.edu)).



## METHODS

**Mice.** All non-transgenic, transgenic and control mice used in this study were derived from in house breeding colonies backcrossed > 12 generations onto C57/BL6 backgrounds. All mice used were young adult females between two and four months old at the time of spinal cord injury. All transgenic mice used have been previously well characterized or are the progeny of crossing well-characterized lines: (1) mGFAP-TK transgenic mice line 7.1<sup>15,16,49</sup>; (2) mGFAP-Cre-STAT3-*loxP* mice generated by crossing STAT3-*loxP* mice with *loxP* sites flanking exon 22 of the STAT3 gene<sup>50</sup> with mGFAP-Cre mice line 73.12<sup>17,18</sup>; (3) *loxP*-STOP-*loxP*-DTR (diphtheria toxin receptor) mice<sup>21</sup>; (4) mGFAP-Cre-RiboTag mice generated by crossing mice with *loxP*-STOP-*loxP*-Rpl22-HA (RiboTag)<sup>26</sup> with mGFAP-Cre mice line 73.12<sup>17,18</sup>; (5) *loxP*-STOP-*loxP*-tdTomato reporter mice<sup>51</sup>. All mice were housed in a 12-h light/dark cycle in a specific-pathogen-free facility with controlled temperature and humidity and were allowed free access to food and water. All experiments were conducted according to protocols approved by the Animal Research Committee of the Office for Protection of Research Subjects at University of California, Los Angeles.

**Surgical procedures.** All surgeries were performed under general anaesthesia with isoflurane in oxygen-enriched air using an operating microscope (Zeiss, Oberkochen, Germany), and rodent stereotaxic apparatus (David Kopf, Tujunga, CA). Laminectomy of a single vertebra was performed and severe crush spinal cord injuries (SCI) were made at the level of T10 using No. 5 Dumont forceps (Fine Science Tools, Foster City, CA) without spacers and with a tip width of 0.5 mm to completely compress the entire spinal cord laterally from both sides for 5 s<sup>16–18</sup>. For pre-conditioning lesions, sciatic nerves were transected and ligated one week before SCI. Hydrogels were injected stereotactically into the centre of SCI lesions 0.6 mm below the surface at 0.2  $\mu$ l per minute using glass micropipettes (ground to 50–100  $\mu$ m tips) connected via high-pressure tubing (Kopf) to 10- $\mu$ l syringes under control of microinfusion pumps, two days after SCI<sup>52</sup>. Tract tracing was performed by injection of biotinylated dextran amine 10,000 (BDA, Invitrogen) 10% wt/vol in sterile saline injected 4  $\times$  0.4  $\mu$ l into the left motor cerebral cortex 14 days before perfusion to visualize corticospinal tract (CST) axons, or cholera toxin B (CTB) (List Biological Laboratory, Campbell, CA) 1  $\mu$ l of 1% wt/vol in sterile water injected into both sciatic nerves three days before perfusion to visualize ascending sensory tract (AST) axons<sup>33</sup>. AAV2/5-GfaABC1D-Cre (see below) was injected either 3 or 6  $\times$  0.4  $\mu$ l (1.29  $\times$  10<sup>13</sup> gc ml<sup>-1</sup> in sterile saline) into and on either side of mature SCI lesions two weeks after SCI, or into uninjured spinal cord after T10 laminectomy. All animals received analgesic before wound closure and every 12 h for at least 48 h post-injury. Animals were randomly assigned numbers and evaluated thereafter blind to genotype and experimental condition.

**AAV2/5-GfaABC1D-Cre.** Adeno-associated virus 2/5 (AAV) vector with a minimal GFAP promoter (AAV2/5 GfaABC1D) was used to target Cre-recombinase expression selectively to astrocytes<sup>53–55</sup>.

**Hydrogel with growth factors and antibodies.** Diblock co-polypeptide hydrogel (DCH) K<sub>180</sub>L<sub>20</sub> was fabricated, tagged with blue fluorescent dye (AMCA-X) and loaded with growth factor and antibody cargoes as described<sup>38,39,52</sup>. Cargo molecules comprised: human recombinant NT3 and BDNF were gifts (Amgen, Thousand Oaks, CA, (NT3 Lot#2200F4; BDNF Lot#2142F5A) or were purchased from PeprroTech (Rocky Hill, NJ; NT3 405-03, Lot#060762; BDNF 405-02 Lot#071161). Function blocking anti-CD29 mouse monoclonal antibody was purchased from BD Bioscience (San Diego, CA) as a custom order at 10.25 mg ml<sup>-1</sup> (product #BP555003; lot#S03146). Freeze dried K<sub>180</sub>L<sub>20</sub> powder was reconstituted on to 3.0% or 3.5% wt/vol basis in sterile PBS without cargo or with combinations of NT3 (1.0  $\mu$ g  $\mu$ l<sup>-1</sup>), BDNF (0.85  $\mu$ g  $\mu$ l<sup>-1</sup>) and anti-CD29 (5  $\mu$ g  $\mu$ l<sup>-1</sup>). DCH mixtures were prepared to have G' (storage modulus at 1 Hz) between 75 and 100 Pascal (Pa), somewhat below that of mouse brain at 200 Pa (refs 38,39).

**Ganciclovir (GCV), BrdU or DT injections.** GCV (Cytovene-IV Hoffman LaRoche, Nutley, NJ), 25 mg kg<sup>-1</sup> per day dissolved in sterile physiological saline was administered as single daily subcutaneous injections starting immediately after surgery and continued for the first 7 days after SCI. Bromodeoxyuridine (BrdU, Sigma), 100 mg kg<sup>-1</sup> per day dissolved in saline plus 0.007 M NaOH, was administered as single daily intraperitoneal injections on days 2 through 7 after SCI. Diphtheria toxin A (DT, Sigma #DO564) 100 ng in 100  $\mu$ l sterile saline was administered twice daily as intraperitoneal injections for ten days starting three weeks after injection of AAV2/5-GfaABC1D-Cre to *loxP*-DTR mice (which was 5 weeks after SCI) (see timeline in Extended Data Fig. 1d).

**Hindlimb locomotor evaluation, animal inclusion criteria, randomization and blinding.** Two days after SCI, all mice were evaluated in open field and mice exhibiting any hindlimb movements were not studied further. Mice that passed this pre-determined inclusion criterion were randomized into experimental groups for further treatments and were thereafter evaluated blind to their

experimental condition. At 3, 7, 14 days and then weekly after SCI, hindlimb movements were scored using a simple six-point scale in which 0 is no movement and 5 is normal walking<sup>17</sup>.

**Histology and immunohistochemistry.** After terminal anaesthesia by barbiturate overdose mice were perfused transcardially with 10% formalin (Sigma). Spinal cords were removed, post-fixed overnight, and cryoprotected in buffered 30% sucrose for 48 h. Frozen sections (30  $\mu$ m horizontal) were prepared using a cryostat microtome (Leica) and processed for immunofluorescence as described<sup>16–18</sup>. Primary antibodies were: rabbit anti-GFAP (1:1,000; Dako, Carpinteria, CA); rat anti-GFAP (1:1,000, Zymed Laboratories); goat anti-CTB (1:1,000, List Biological Lab); rabbit anti-5HT (1:2,000, Immunostar); goat anti-5HT (1:1,000, Immunostar); mouse anti-CSPG<sup>22</sup> (1:100, Sigma); rabbit-anti haemagglutinin (HA) (1:500 Sigma); mouse-anti HA (1:3,000 Covance); sheep anti-BrdU (1:6,000, Maine Biotechnology Services, Portland, ME); rabbit anti-laminin (1:80, Sigma, Saint Louis, MO); guinea pig anti-NG2 (CSPG4) (E. G. Hughes and D. W. Bergles<sup>56</sup>, Baltimore, MA); goat anti-aggrexin (1:200, NOVUS); rabbit anti-brevican (1:300, NOVUS); mouse anti-neurocan (1:300, Milipore); mouse anti-phosphacan (1:500, Sigma); goat anti-versican (1:200, NOVUS); rabbit anti-neuronal C (CSPG5) (1:200, NOVUS). Fluorescence secondary antibodies were conjugated to: Alexa 488 (green) or Alexa 350 (blue) (Molecular Probes), or to Cy3 (550, red) or Cy5 (649, far red) all from (Jackson ImmunoResearch Laboratories). Mouse primary antibodies were visualized using the Mouse-on-Mouse detection kit (M.O.M., Vector). BDA tract-tracing was visualized with streptavidin-HRP plus TSB Fluorescein green or Tyr-Cy3 (Jackson ImmunoResearch Laboratories). Nuclear stain: 4',6'-diamidino-2-phenylindole dihydrochloride (DAPI; 2 ng ml<sup>-1</sup>; Molecular Probes). Sections were coverslipped using ProLong Gold anti-fade reagent (Invitrogen, Grand Island, NY). Sections were examined and photographed using deconvolution fluorescence microscopy and scanning confocal laser microscopy (Zeiss, Oberkochen, Germany).

**Axon quantification.** Axons labelled by tract tracing or immunohistochemistry were quantified using image analysis software (NeuroLucida, MicroBrightField, Williston, VT) operating a computer-driven microscope regulated in the x, y and z axes (Zeiss) by observers blind to experimental conditions. Using NeuroLucida, lines were drawn across horizontal spinal cord sections at SCI lesion centres and at regular distances on either side (Fig. 1a) and the number of axons intercepting lines was counted at 63 $\times$  magnification under oil immersion by observers blind to experimental conditions. Similar lines were drawn and axons counted in intact axon tracts 3 mm proximal to SCI lesions and the numbers of axon intercepts in or near lesions were expressed as percentages of axons in the intact tracts in order to control for potential variations in tract-tracing efficacy or intensity of immunohistochemistry among animals. Two sections at the level of the CST or AST, and three sections through the middle of the cord for 5HT, were counted per mouse and expressed as total intercepts per location per mouse. To determine efficacy of axon transection after SCI, we examined labelling 3 mm distal to SCI lesion centres, with the intention of eliminating mice that had labelled axons at this location on grounds that these mice may have had incomplete lesions. However, all mice that had met the strict behavioural inclusion criterion of no hindlimb movements two days after severe crush SCI, exhibited no detectable axons 3 mm distal to SCI lesions regardless of treatment group.

**Quantification of immunohistochemically stained areas.** Sections stained for GFAP, CSPG or laminin were photographed using constant exposure settings. Single-channel immunofluorescence images were converted to black and white and thresholded (Fig. 1d and Extended Data Fig. 2b) and the amount of stained area measured in different tissue compartments using NIH ImageJ software. Areas are shown in graphs as mean values plus or minus standard error of the means (s.e.m.).

**Statistics, power calculations and group sizes.** Statistical evaluations of repeated measures were conducted by ANOVA with post hoc, independent pairwise analysis as per Newman-Keuls (Prism, GraphPad, San Diego, CA). Power calculations were performed using G\*Power Software v3.1.9.2 (ref. 57). For quantification of histologically derived neuroanatomical outcomes such as numbers of axons or percentage of area stained for GFAP or CSPG, group sizes were used that were calculated to provide at least 80% power when using the following parameters: probability of type I error ( $\alpha$ ) = 0.05, a conservative effect size of 0.25, 2–8 treatment groups with multiple measurements obtained per replicate. Using Fig. 5j as an example, evaluation of  $n = 5$  biological replicates (with multiple measurements per replicate) in each of 8 treatment groups provided greater than 88% power.

**Dot blot.** For dot blot immunoassay of chondroitin sulfate proteoglycans (CSPG), spinal cord tissue blocks were lysed and homogenized in standard RIPA (radio-immunoprecipitation assay) buffer. LDS (lithium dodecyl sulfate) buffer (Life Technologies) was added to the post-mitochondrial supernatant and 2  $\mu$ l containing 2  $\mu$ g  $\mu$ l<sup>-1</sup> protein was spotted onto a nitrocellulose membrane

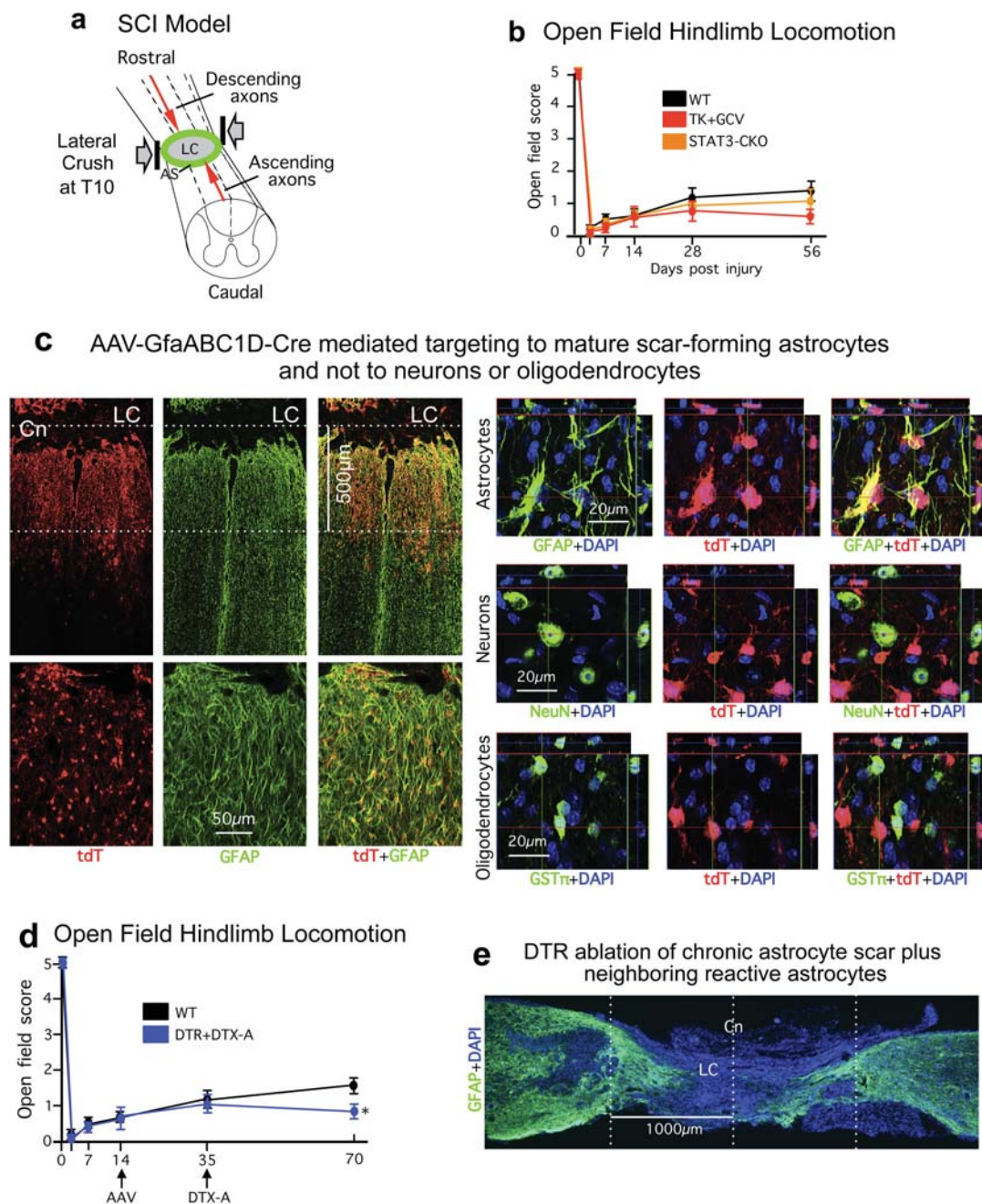
(Life Technologies), set to dry and incubated overnight with mouse anti-chondroitin sulfate antibody (CS56, 1:1000, Sigma Aldrich), an IgM-monoclonal antibody that detects glyco-moieties of all CSPGs<sup>22</sup>. CS56 immunoreactivity was detected on X-ray film with alkaline phosphatase-conjugated secondary antibody and chemiluminescent substrate (Life Technologies). Densitometry measurements of CS56 immunoreactivity were obtained using ImageJ software (NIH) and normalized to total protein (Ponceau S) density<sup>58</sup>. Densities are shown in graphs as mean values plus or minus standard error of the means (s.e.m.).

**Isolation, sequencing and analysis of RNA from astrocytes and non-astrocyte cells.** Two weeks after SCI, spinal cords of wild-type control (GFAP-RiboTag) and STAT3-CKO (GFAP-STAT3CKO-RiboTag) mice were rapidly dissected out of the spinal canal. The central 3 mm of the lower thoracic lesion including the lesion core and 1 mm rostral and caudal were then rapidly removed and snap frozen in liquid nitrogen. Haemagglutinin (HA) immunoprecipitation (HA-IP) of astrocyte ribosomes and ribosome-associated mRNA (ramRNA) was carried out as described<sup>26</sup>. The non-precipitated flow-through (FT) from each IP sample was collected for analysis of non-astrocyte total RNA. HA and FT samples underwent on-column DNA digestion using the RNase-Free Dnase Set (Qiagen) and RNA purified with the RNeasy Micro kit (Qiagen). Integrity of the eluted RNA was analysed by a 2100 Bioanalyzer (Agilent) using the RNA Pico chip, mean sample RIN =  $8.0 \pm 0.95$ . RNA concentration determined by RiboGreen RNA Assay kit (Life Technologies). cDNA was generated from 5 ng of IP or FT RNA using the Nugen Ovation 2 RNA-Seq System V2 kit (Nugen). 1 µg of cDNA was fragmented using the Covaris M220. Paired-end libraries for multiplex sequencing were generated from 300 ng of fragmented cDNA using the Apollo 324 automated library preparation system (Wafergen Biosystems) and purified with Agencourt AMPure XP beads (Beckman Coulter). All samples were analysed by an Illumina NextSeq 500 Sequencer (Illumina) using 75-bp paired-end sequencing. Reads were quality controlled using in-house scripts including picard-tools, mapped to the reference mm10 genome using STAR<sup>59</sup>, and counted using HT-seq<sup>60</sup> with mm10 refSeq as reference, and genes were called differentially expressed using edgeR<sup>61</sup>. Individual gene expression levels in the Fig. 4e histogram are shown as mean FPKM (fragments per kilobase of transcript sequence per million mapped fragments). Additional details of differential expression analysis are described in the legends of Fig. 4 and Extended Data Figs 3 and 4. Raw and normalized data have been deposited in the NCBI Gene Expression Omnibus and are accessible through accession number GSE76097. To ensure the widespread distribution of these datasets, we have created a user-friendly website that enables searching for individual genes of interest <https://astrocyte.rnaseq.sofroniewlab.neurobio.ucla.edu>.

49. Bush, T. G. *et al.* Fulminant jejuno-ileitis following ablation of enteric glia in adult transgenic mice. *Cell* **93**, 189–201 (1998).
50. Takeda, K. *et al.* Stat3 activation is responsible for IL-6-dependent T cell proliferation through preventing apoptosis: generation and characterization of T cell-specific Stat3-deficient mice. *J. Immunol.* **161**, 4652–4660 (1998).
51. Madisen, L. *et al.* A robust and high-throughput Cre reporting and characterization system for the whole mouse brain. *Nature Neurosci.* **13**, 133–140 (2010).
52. Zhang, S. *et al.* Tunable diblock copolymer hydrogel depots for local delivery of hydrophobic molecules in healthy and injured central nervous system. *Biomaterials* **35**, 1989–2000 (2014).
53. Shigetomi, E. *et al.* Imaging calcium microdomains within entire astrocyte territories and endfeet with GCaMPs expressed using adeno-associated viruses. *J. Gen. Physiol.* **141**, 633–647 (2013).
54. Jiang, R., Haustein, M. D., Sofroniew, M. V. & Khakh, B. S. Imaging intracellular Ca<sup>2+</sup> signals in striatal astrocytes from adult mice using genetically-encoded calcium indicators. *J. Vis. Exp.* **93**, e51972 (2014).
55. Tong, X. *et al.* Astrocyte Kir4.1 ion channel deficits contribute to neuronal dysfunction in Huntington's disease model mice. *Nature Neurosci.* **17**, 694–703 (2014).
56. Kang, S. H. *et al.* Degeneration and impaired regeneration of gray matter oligodendrocytes in amyotrophic lateral sclerosis. *Nature Neurosci.* **16**, 571–579 (2013).
57. Faul, F., Erdfelder, E., Lang, A. G. & Buchner, A. G. \*Power 3: a flexible statistical power analysis program for the social, behavioral, and biomedical sciences. *Behav. Res. Methods* **39**, 175–191 (2007).
58. Romero-Calvo, I. *et al.* Reversible Ponceau staining as a loading control alternative to actin in western blots. *Anal. Biochem.* **401**, 318–320 (2010).
59. Dobin, A. *et al.* STAR: ultrafast universal RNA-seq aligner. *Bioinformatics* **29**, 15–21 (2013).
60. Anders, S., Pyl, P. T. & Huber, W. HTSeq—a Python framework to work with high-throughput sequencing data. *Bioinformatics* **31**, 166–169 (2015).
61. Robinson, M. D., McCarthy, D. J. & Smyth, G. K. edgeR: a Bioconductor package for differential expression analysis of digital gene expression data. *Bioinformatics* **26**, 139–140 (2010).
62. Friedlander, D. R. *et al.* The neuronal chondroitin sulfate proteoglycan neurocan binds to the neural cell adhesion molecules Ng-CAM/L1/NILE and N-CAM, and inhibits neuronal adhesion and neurite outgrowth. *J. Cell Biol.* **125**, 669–680 (1994).
63. Sango, K. *et al.* Phosphacan and neurocan are repulsive substrata for adhesion and neurite extension of adult rat dorsal root ganglion neurons in vitro. *Exp. Neurol.* **182**, 1–11 (2003).
64. Hurtado, A., Podinin, H., Oudega, M. & Grimpel, B. Deoxyribozyme-mediated knockdown of xylosyltransferase-1 mRNA promotes axon growth in the adult rat spinal cord. *Brain* **131**, 2596–2605 (2008).
65. Becker, C. G., Schweitzer, J., Feldner, J., Becker, T. & Schachner, M. Tenascin-R as a repellent guidance molecule for developing optic axons in zebrafish. *J. Neurosci.* **23**, 6232–6237 (2003).
66. Dickson, B. J. Molecular mechanisms of axon guidance. *Science* **298**, 1959–1964 (2002).
67. Masuda, T. *et al.* Netrin-1 acts as a repulsive guidance cue for sensory axonal projections toward the spinal cord. *J. Neurosci.* **28**, 10380–10385 (2008).
68. Winberg, M. L. *et al.* Plexin A is a neuronal semaphorin receptor that controls axon guidance. *Cell* **95**, 903–916 (1998).
69. Hu, H., Marton, T. F. & Goodman, C. S. Plexin B mediates axon guidance in *Drosophila* by simultaneously inhibiting active Rac and enhancing RhoA signaling. *Neuron* **32**, 39–51 (2001).
70. He, Z. & Tessier-Lavigne, M. Neuropilin is a receptor for the axonal chemorepellent Semaphorin III. *Cell* **90**, 739–751 (1997).
71. Lu, X. *et al.* The netrin receptor UNC5B mediates guidance events controlling morphogenesis of the vascular system. *Nature* **432**, 179–186 (2004).
72. Keino-Masu, K. *et al.* Deleted in Colorectal Cancer (DCC) encodes a netrin receptor. *Cell* **87**, 175–185 (1996).
73. Ahmed, G. *et al.* Draxin inhibits axonal outgrowth through the netrin receptor DCC. *J. Neurosci.* **31**, 14018–14023 (2011).
74. Rajagopalan, S. *et al.* Neogenin mediates the action of repulsive guidance molecule. *Nature Cell Biol.* **6**, 756–762 (2004).
75. Monnier, P. P. *et al.* RGM is a repulsive guidance molecule for retinal axons. *Nature* **419**, 392–395 (2002).
76. Kajiwara, Y., Buxbaum, J. D. & Grice, D. E. SLITRK1 binds 14-3-3 and regulates neurite outgrowth in a phosphorylation-dependent manner. *Biol. Psychiatry* **66**, 918–925 (2009).
77. Islam, S. M. *et al.* Draxin, a repulsive guidance protein for spinal cord and forebrain commissures. *Science* **323**, 388–393 (2009).
78. Yang, Z. *et al.* NG2 glial cells provide a favorable substrate for growing axons. *J. Neurosci.* **26**, 3829–3839 (2006).
79. Hossain-Ibrahim, M. K., Rezakooi, K., Stallcup, W. B., Lieberman, A. R. & Anderson, P. N. Analysis of axonal regeneration in the central and peripheral nervous systems of the NG2-deficient mouse. *BMC Neurosci.* **8**, 80 (2007).
80. Lu, P., Jones, L. L. & Tuszynski, M. H. Axon regeneration through scars and into sites of chronic spinal cord injury. *Exp. Neurol.* **203**, 8–21 (2007).
81. Busch, S. A. *et al.* Adult NG2+ cells are permissive to neurite outgrowth and stabilize sensory axons during macrophage-induced axonal dieback after spinal cord injury. *J. Neurosci.* **30**, 255–265 (2010).
82. Nakanishi, K. *et al.* Identification of neurite outgrowth-promoting domains of neuroglycan C, a brain-specific chondroitin sulfate proteoglycan, and involvement of phosphatidylinositol 3-kinase and protein kinase C signaling pathways in neurite outgrowth. *J. Biol. Chem.* **281**, 24970–24978 (2006).
83. Götz, B. *et al.* Tenascin-C contains distinct adhesive, anti-adhesive, and neurite outgrowth promoting sites for neurons. *J. Cell Biol.* **132**, 681–699 (1996).
84. Andrews, M. R. *et al.* Alpha9 integrin promotes neurite outgrowth on tenascin-C and enhances sensory axon regeneration. *J. Neurosci.* **29**, 5546–5557 (2009).
85. Edwards, T. J. & Hammarlund, M. Syndecan promotes axon regeneration by stabilizing growth cone migration. *Cell Rep.* **8**, 272–283 (2014).
86. Farhy Tselnicker, I., Boisvert, M. M. & Allen, N. J. The role of neuronal versus astrocyte-derived heparan sulfate proteoglycans in brain development and injury. *Biochem. Soc. Trans.* **42**, 1263–1269 (2014).
87. Lu, P., Jones, L. L. & Tuszynski, M. H. BDNF-expressing marrow stromal cells support extensive axonal growth at sites of spinal cord injury. *Exp. Neurol.* **191**, 344–360 (2005).
88. Grill, R., Murai, K., Blesch, A. & Tuszynski, M. H. Cellular delivery of neurotrophin-3 promotes corticospinal axonal growth and partial functional recovery after spinal cord injury. *J. Neurosci.* **17**, 5560–5572 (1997).
89. Blesch, A. & Tuszynski, M. H. Cellular GDNF delivery promotes growth of motor and dorsal column sensory axons after partial and complete spinal cord transections and induces remyelination. *J. Comp. Neurol.* **467**, 403–417 (2003).
90. Blesch, A. *et al.* Leukemia inhibitory factor augments neurotrophin expression and corticospinal axon growth after adult CNS injury. *J. Neurosci.* **19**, 3556–3566 (1999).
91. Cafferty, W. B. *et al.* Leukemia inhibitory factor determines the growth status of injured adult sensory neurons. *J. Neurosci.* **21**, 7161–7170 (2001).
92. Müller, A., Hauk, T. G. & Fischer, D. Astrocyte-derived CNTF switches mature RGCs to a regenerative state following inflammatory stimulation. *Brain* **130**, 3308–3320 (2007).
93. Ozdinler, P. H. & Macklis, J. D. IGF-I specifically enhances axon outgrowth of corticospinal motor neurons. *Nature Neurosci.* **9**, 1371–1381 (2006).



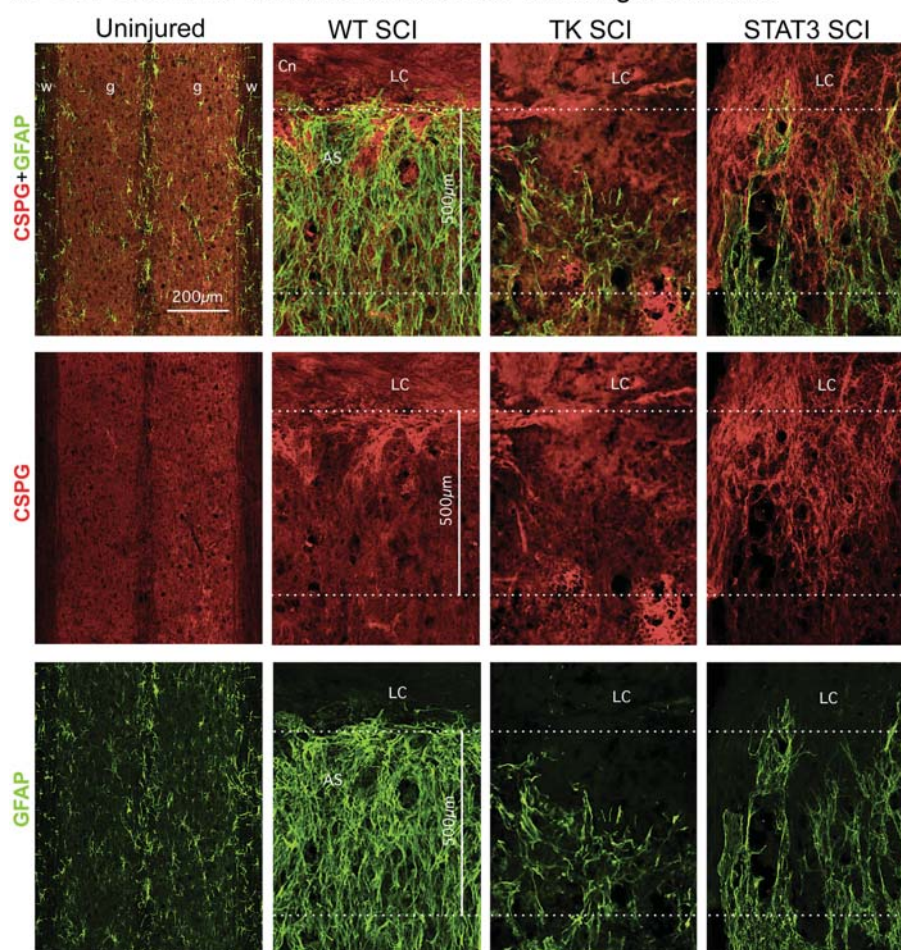
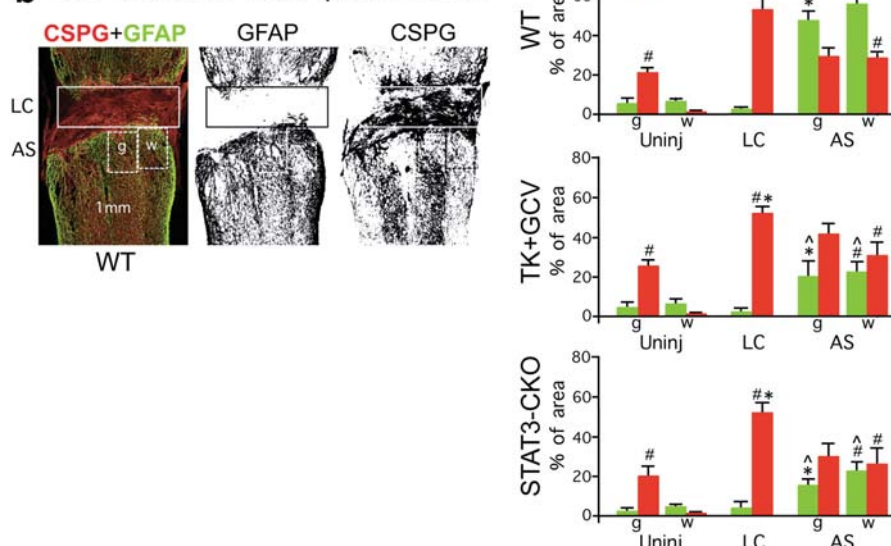
94. Szebenyi, G. *et al.* Fibroblast growth factor-2 promotes axon branching of cortical neurons by influencing morphology and behavior of the primary growth cone. *J. Neurosci.* **21**, 3932–3941 (2001).
95. White, R. E., Yin, F. Q. & Jakeman, L. B. TGF- $\alpha$  increases astrocyte invasion and promotes axonal growth into the lesion following spinal cord injury in mice. *Exp. Neurol.* **214**, 10–24 (2008).
96. Tom, V. J., Doller, C. M., Malouf, A. T. & Silver, J. Astrocyte-associated fibronectin is critical for axonal regeneration in adult white matter. *J. Neurosci.* **24**, 9282–9290 (2004).
97. Qin, J., Liang, J. & Ding, M. Perlecan antagonizes collagen IV and ADAMTS9/GON-1 in restricting the growth of presynaptic boutons. *J. Neurosci.* **34**, 10311–10324 (2014).
98. Hill, J. J., Jin, K., Mao, X. O., Xie, L. & Greenberg, D. A. Intracerebral chondroitinase ABC and heparan sulfate proteoglycan glypican improve outcome from chronic stroke in rats. *Proc. Natl Acad. Sci. USA* **109**, 9155–9160 (2012).
99. Minor, K. *et al.* Decorin promotes robust axon growth on inhibitory CSPGs and myelin via a direct effect on neurons. *Neurobiol. Dis.* **32**, 88–95 (2008).
100. Horie, H. *et al.* Galectin-1 regulates initial axonal growth in peripheral nerves after axotomy. *J. Neurosci.* **19**, 9964–9974 (1999).
101. Walsh, F. S. & Doherty, P. Neural cell adhesion molecules of the immunoglobulin superfamily: role in axon growth and guidance. *Annu. Rev. Cell Dev. Biol.* **13**, 425–456 (1997).
102. Malin, D. *et al.* The extracellular-matrix protein matrilin 2 participates in peripheral nerve regeneration. *J. Cell Sci.* **122**, 995–1004 (2009).
103. Zhang, Y. *et al.* An RNA-sequencing transcriptome and splicing database of glia, neurons, and vascular cells of the cerebral cortex. *J. Neurosci.* **34**, 11929–11947 (2014).



**Extended Data Figure 1 | SCI model schematic, locomotor behavioural effects, and AAV vector targeting specificity and effects.** **a**, Schematic of severe lateral crush SCI at thoracic level T10 that generates a large lesion core (LC) of non-neural tissue surrounded by an astrocytic scar (AS) and completely transects descending and ascending axons. **b**, Open field hindlimb locomotor score at various times after SCI assessed using a 5-point scale where 5 is normal and 0 is no movement of any kind<sup>17</sup>. No significant differences were observed among any of the experimental groups at any time point.  $n = 6$  mice at all time points  $P > 0.5$  (ANOVA with Newman–Keuls post hoc analysis). WT, wild type. **c**, Horizontal sections through a severe SCI lesion of a representative tdTomato (tdT) reporter mouse<sup>51</sup> injected with an AAV vector with a minimal *Gfap* promoter regulating Cre (AAV2/5-GfaABC1D-Cre) into the lesion at two weeks after SCI and perfused at three weeks. tdTomato labelling demonstrates that this AAV2/5-GfaABC1D-Cre efficiently and specifically targets GFAP-positive astrocytes. In this mouse, the amount AAV2/5-GfaABC1D-Cre injected was intentionally titrated on the basis of previous trial and error to target primarily the astrocytic scar border in an approximately 500µm zone immediately abutting the SCI lesion core. High-magnification analysis of individual fluorescence channels stained for tdTomato plus various cell markers shows the specificity of Cre activity targeting to cells

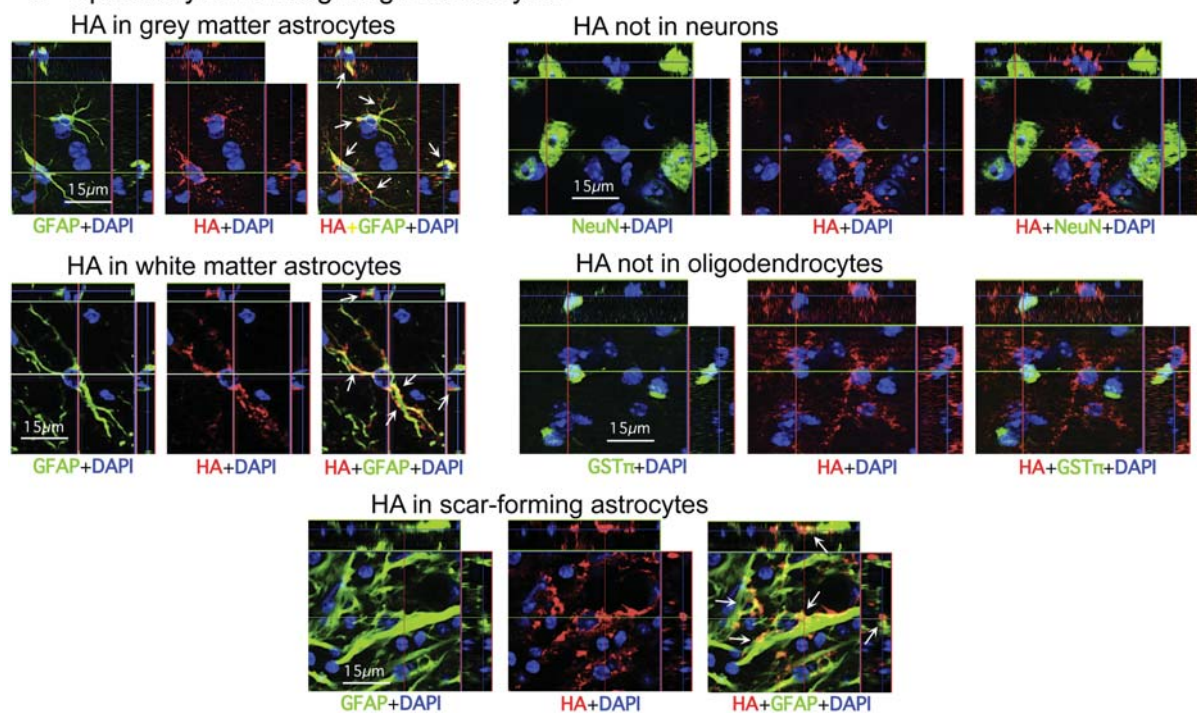
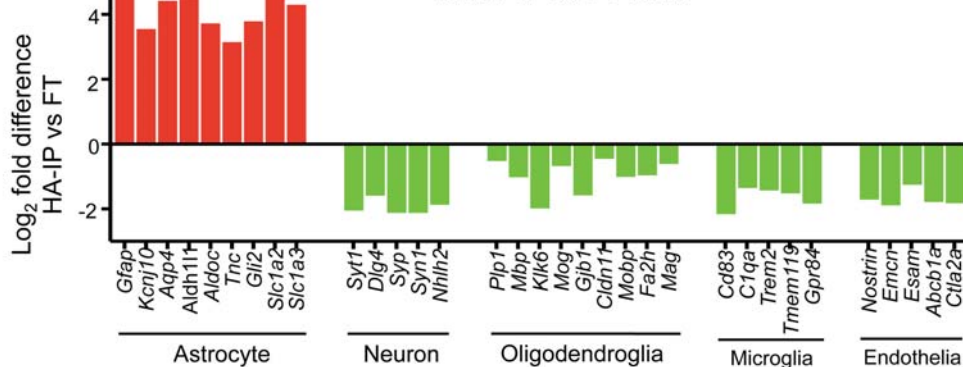
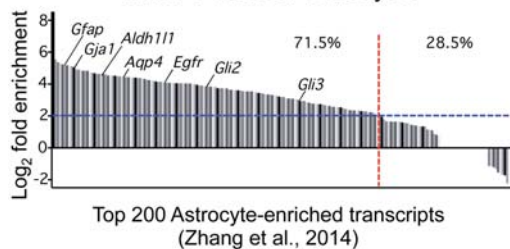
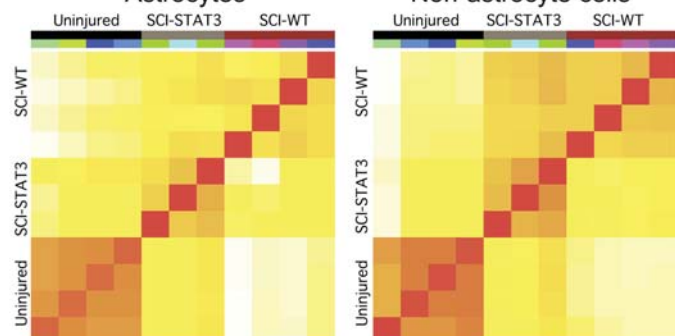
expressing the astrocyte marker, GFAP, but not to cells expressing either the neuronal marker, NeuN, or the mature oligodendrocyte marker, GST $\pi$ . AAV2/5-GfaABC1D-Cre was prepared using a previously described and well-characterized cloning strategy<sup>53–55</sup>. **d**, Open field hindlimb locomotor scores at various times after SCI. There was no difference in scores of control mice and *loxP*-STOP-*loxP*-DTR (diphtheria toxin receptor) mice that received AAV2/5-GfaABC1D-Cre before injections of diphtheria toxin (DT). Five weeks after DT injections, *loxP*-DTR mice that received AAV2/5-GfaABC1D-Cre exhibited a slightly, but significantly, lower locomotor score. Hindlimb locomotion was assessed using a 5-point scale where 5 is normal and 0 is no movement of any kind<sup>17</sup>.  $n = 6$  mice per group;  $*P < 0.05$  versus wild-type (ANOVA with Newman–Keuls). **e**, GFAP immunohistochemistry of a sagittal section after ablation of a chronic astrocytic scar plus adjacent astrocytes. DT was administered to a transgenic mouse expressing DTR targeted selectively to astrocytes around a severe SCI. In this case, the amount of AAV2/5-GfaABC1D-Cre injected was titrated to target not only primarily the astrocytic scar border but also adjacent astrocytes spread over approximately 2 mm on either side of the centre (Cn) of the SCI lesion core (LC). Note the profound degeneration of neural tissue resulting from the selective ablation of the chronic astrocytic scar plus adjacent astrocytes after SCI.



**a** CSPG & GFAP immunofluorescence with single channels**b** CSPG & GFAP area quantification

**Extended Data Figure 2 | Single-channel CSPG and GFAP immunofluorescence and stained area quantification.** **a**, Individual fluorescence channels of CS56 and GFAP immunohistochemistry from horizontal sections of uninjured mice and at two weeks after severe SCI shown in Fig. 3b. Sections are taken from wild-type (WT) mice and mice with transgenic ablation (TK+GCV) or attenuation (STAT3-CKO) of astrocytic scar formation. **b**, Example of black and white thresholding of single channels of immunofluorescence staining for image analysis to quantify (using NIH Image J software) the amount of CSPG- or

GFAP-stained area in different tissue compartments in SCI lesions. Boxes denote areas quantified to obtain values for lesion core (LC) and grey (g) or white (w) matter in astrocytic scar (AS) or equivalent regions in uninjured tissue. Graphs show percentage of areas (means  $\pm$  s.e.m.) stained for CSPG or GFAP determined using ImageJ.  $n = 4$  (wild type mice);  $n = 6$  (TK+GCV and STAT3-CKO mice);  $\#P < 0.05$  versus uninjured white matter;  $*P < 0.05$  versus uninjured grey matter in same experimental group (ANOVA with Newman-Keuls);  $^{\wedge}P < 0.05$  versus equivalent anatomical region in wild-type (ANOVA with Newman-Keuls).

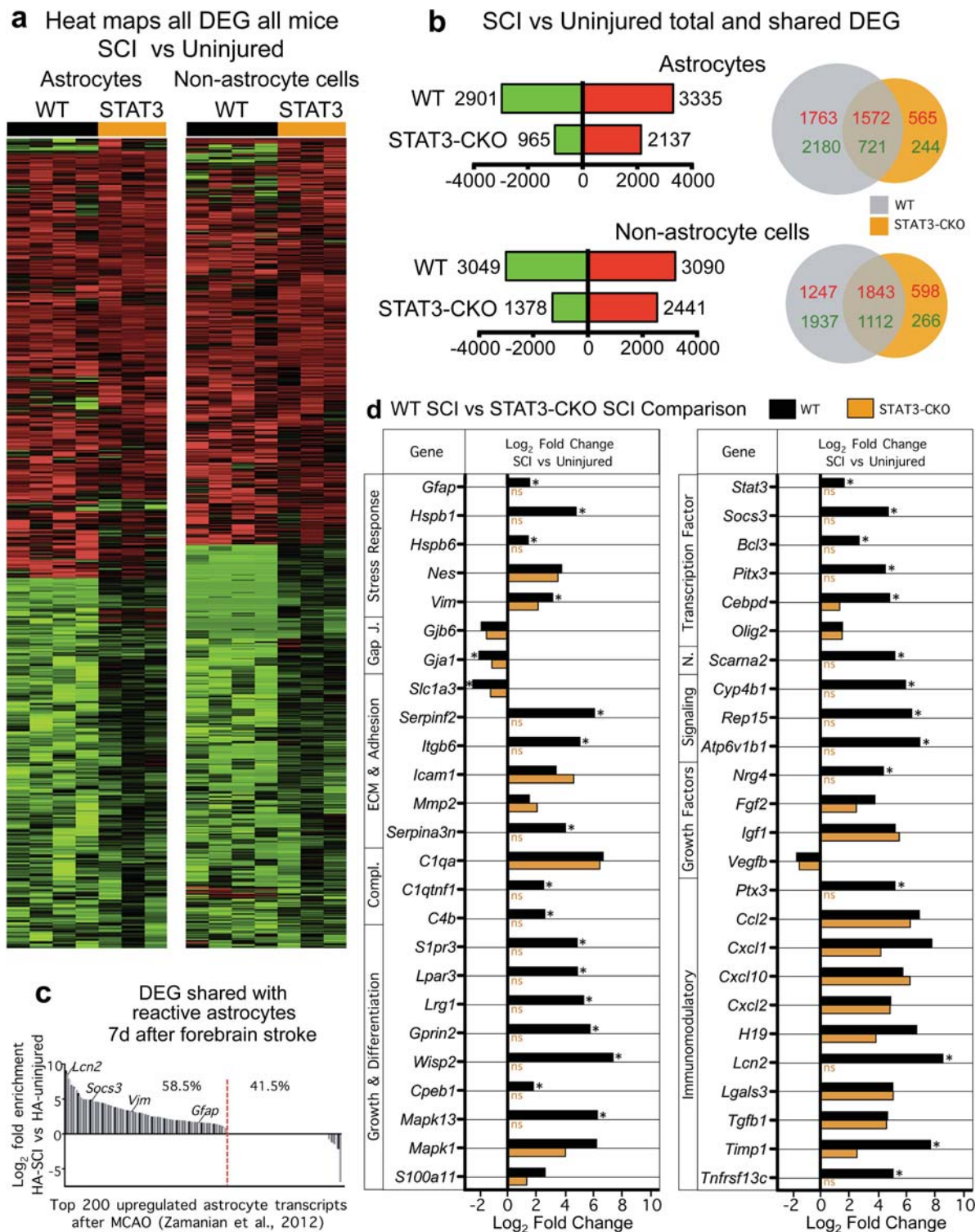
**a** Specificity of HA targeting to astrocytes**b** Enrichment & de-enrichment of cell type-specific transcripts in HA-IP vs FT RNA**c** HA-IP vs FT enrichment shared with P7 cortical astrocytes**d** Pairwise comparisons

Extended Data Figure 3 | See next page for caption.



**Extended Data Figure 3 | Specificity of haemagglutinin targeting to astrocytes and enrichment of haemagglutinin immunoprecipitation for astrocyte-specific RNA transcripts.** **a**, Individual fluorescence channels of immunohistochemistry for transgenically targeted haemagglutinin (HA) plus various cell markers showing the specificity of HA targeting to cells expressing the astrocyte marker, GFAP, and not to cells expressing either the neuronal marker, NeuN, or the mature oligodendrocyte marker, GST $\pi$ , in uninjured grey and white matter and in astrocytic scars at 2 weeks after SCI. **b**, CNS-cell-type-specific gene transcript enrichment of ribosome-associated mRNA (ramRNA) isolated from wild-type (WT) uninjured spinal cord by HA immunoprecipitation (HA-IP). Differential expression analysis by RNA-seq indicates significant enrichment (red) for astrocyte-specific gene transcripts, and de-enrichment (green) for gene transcripts enriched in other CNS cell types, FDR < 0.1. A log<sub>2</sub> scale is used so that positive and negative differences are directly comparable. The mean numerical enrichment of three quintessential astrocyte genes,

*Gfap*, *Aldh1l1* and *Aqp4*, is 25-fold greater in HA samples than in flow-through samples. **c**, Gene transcript enrichment of HA-IP ramRNA relative to P7 mouse primary cortical astrocytes<sup>103</sup>. Of the 200 most highly expressed genes previously described<sup>103</sup> for post-natal mouse cortical astrocytes, 71.5% (red line) are at least fourfold enriched (blue line) in HA-IP ramRNA isolated from uninjured spinal cord relative to flow-through RNA from non-astrocyte cells. **d**, Pearson correlation plots of total normalized RNA-seq reads from individual biological replicates for each treatment condition. Correlation colouring indicates little (white) to high (red) similarity.  $n = 4$  mice each for uninjured controls and wild-type SCI (SCI-WT);  $n = 3$  mice for STAT3-CKO SCI (SCI-STAT3). FDR < 0.1 for differential expression and enrichment analysis. Raw and normalized data have been deposited in the NCBI Gene Expression Omnibus and are accessible through GEO Series accession number GSE76097 and via a searchable, open-access website <https://astrocyte.rnaseq.sofroniewlab.neurobio.ucla.edu>.

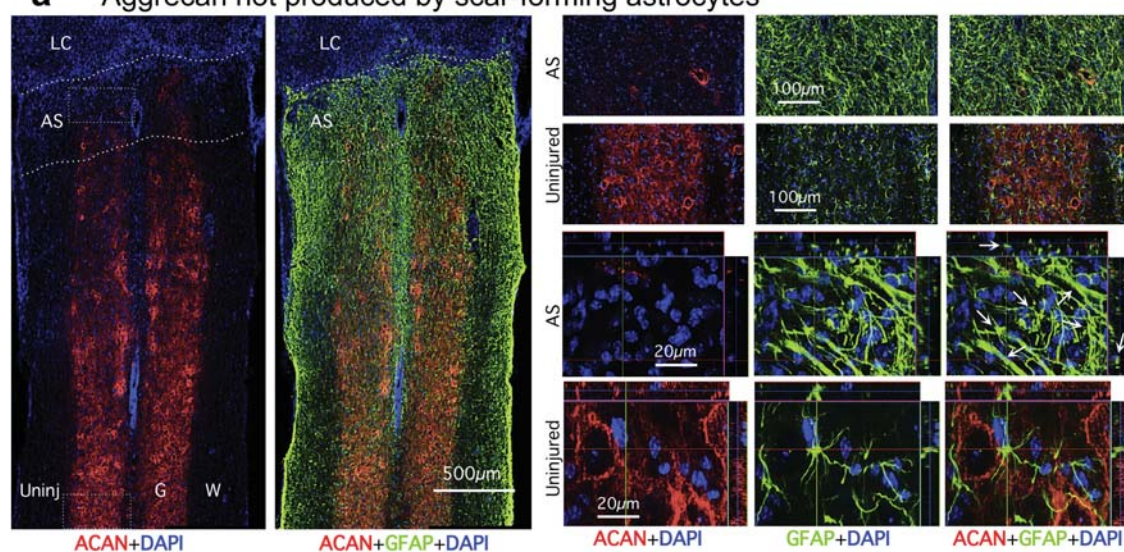
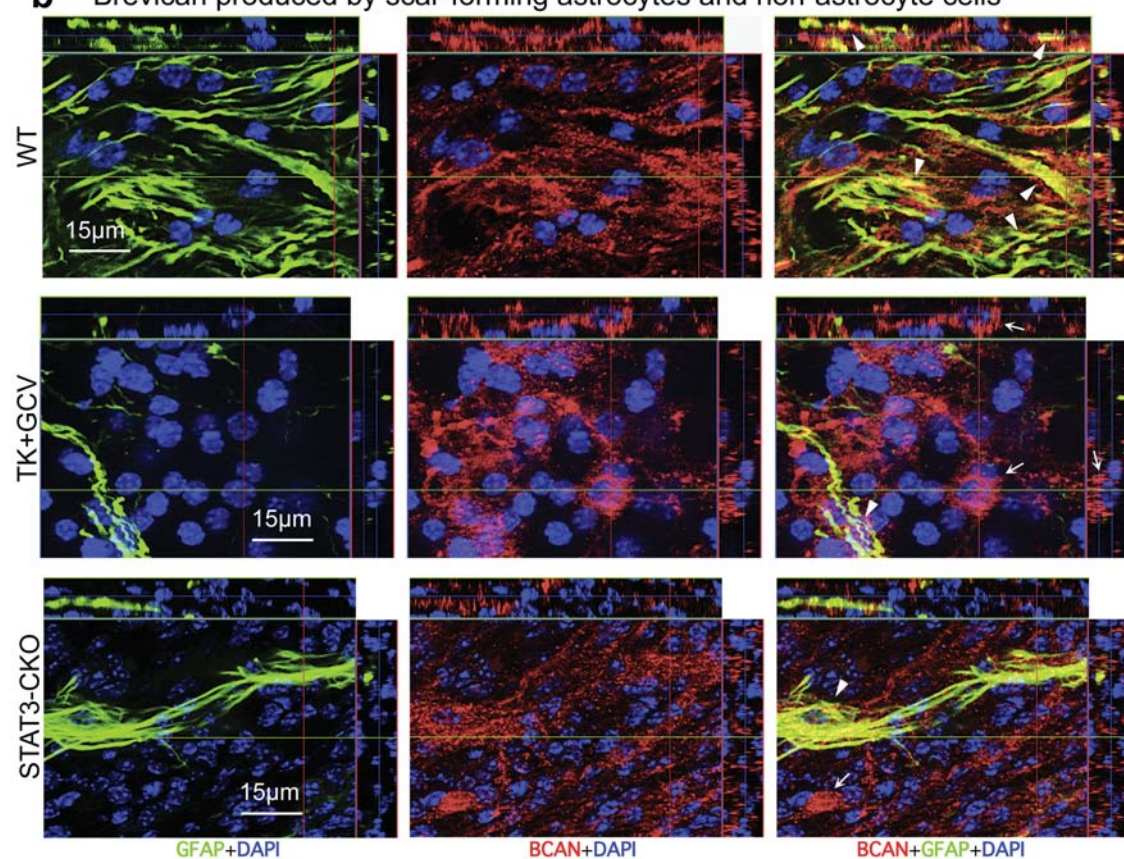


**Extended Data Figure 4 | Comparison of genomic data from astrocytes and non-astrocyte cells from WT and STAT3-CKO mice after SCI.**

**a**, Heat maps depicting all significantly differentially expressed genes (DEG), as determined by RNA-seq, for wild-type (WT) and STAT3-CKO astrocytes and non-astrocytes from independent biological replicates two weeks after SCI relative to uninjured wild-type control. Red upregulated, green downregulated. **b**, Total numbers and Venn diagrams of significant DEGs in wild-type and STAT3-CKO astrocytes and non-astrocytes two weeks after SCI relative to uninjured control. Red and green numerical values indicate significantly upregulated and downregulated genes, respectively. **c**, Comparison of altered gene expression in our SCI-reactive astrocytes and previously reported forebrain stroke-reactive astrocytes<sup>27</sup>.

Of the 200 most highly elevated genes in forebrain astrocytes one week following stroke<sup>27</sup>, 58.5% (red line) are also significantly elevated in astrocytes after SCI, relative to uninjured. **d**, Comparison of expression by wild-type SCI and STAT3-CKO SCI reactive astrocytes of a selected cross-section of genes that are highly regulated after SCI by wild-type reactive astrocytes. Many of the regulated genes exhibit changes that are expected and implicated in wild-type reactive astrogliosis mechanisms and roles, and some of the changes appear to be newly identified in this context. Note that many of the genes are not regulated or exhibit attenuated changes in STAT3-CKO SCI astrocytes.  $n = 4$  mice each for uninjured and wild-type SCI;  $n = 3$  mice for STAT3-CKO SCI (SCI-STAT3). FDR < 0.1 for differential expression and enrichment analysis.

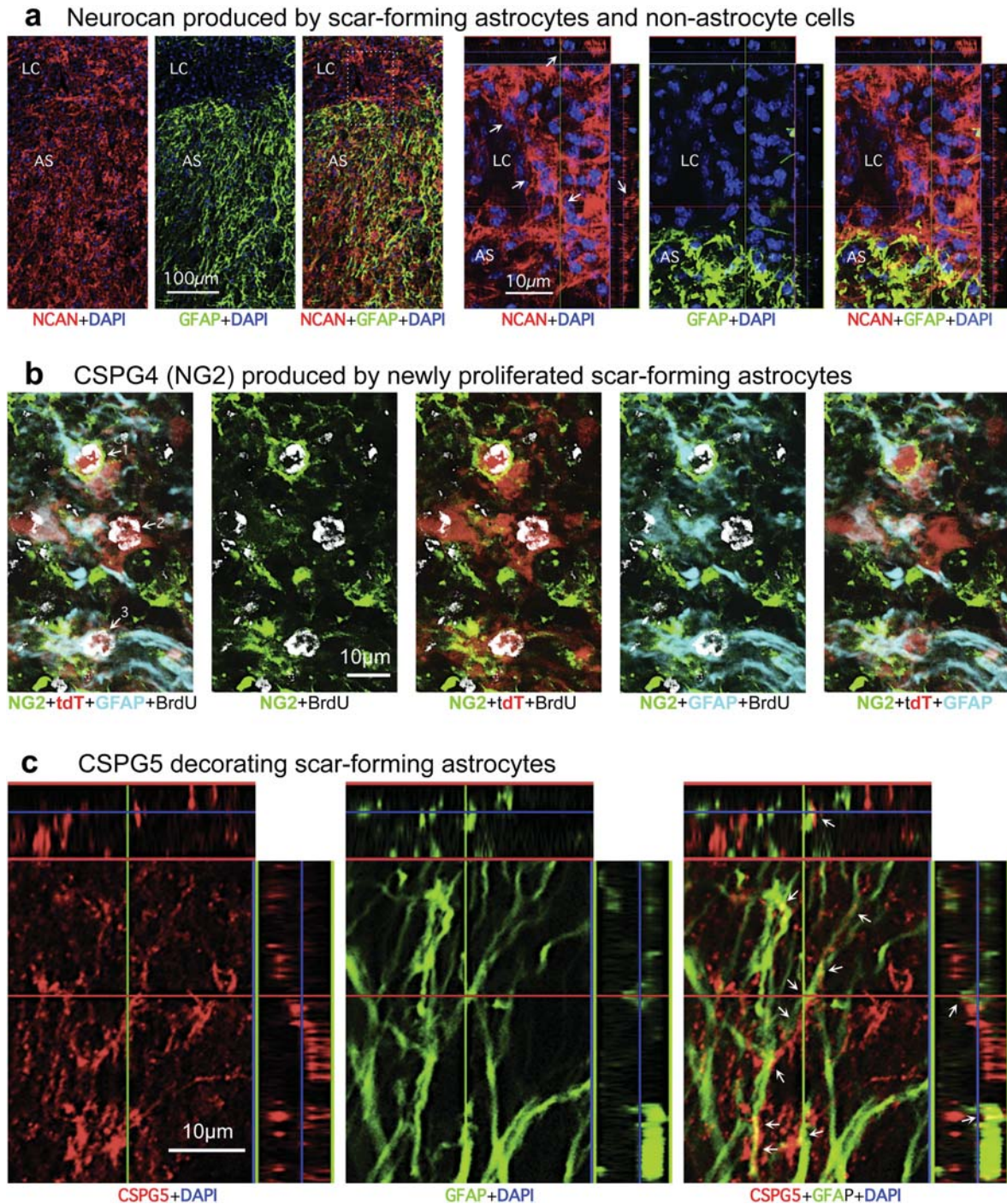


**a** Aggrecan not produced by scar-forming astrocytes**b** Brevican produced by scar-forming astrocytes and non-astrocyte cells

**Extended Data Figure 5 | Immunohistochemistry of specific CSPGs.**  
**a,** Absence of aggrecan (ACAN) production by scar-forming astrocytes. Images show individual fluorescence channels of ACAN and GFAP immunohistochemistry from horizontal sections two weeks after severe SCI in a representative wild-type (WT) mouse. Boxes denote areas of astrocytic scar (AS) or uninjured tissue (Uninj) shown at higher magnification. Note that ACAN is: (i) heavily present in the perineuronal nets that surround neurons in uninjured tissue; (ii) almost absent from astrocytic scar and lesion core (LC); and (iii) not detectably produced

by newly generated scar-forming astrocytes (arrows). **b,** Brevican (BCAN) production by scar-forming astrocytes and non-astrocyte cells. Images show individual fluorescence channels of BCAN and GFAP immunohistochemistry from horizontal sections two weeks after severe SCI, in wild-type mice and mice with transgenic ablation (TK+GCV) or attenuation (STAT3-CKO) of astrocytic scar formation. Note that BCAN is produced both by GFAP-positive scar-forming astrocytes (arrowheads) and by non-astrocyte cells (arrows).

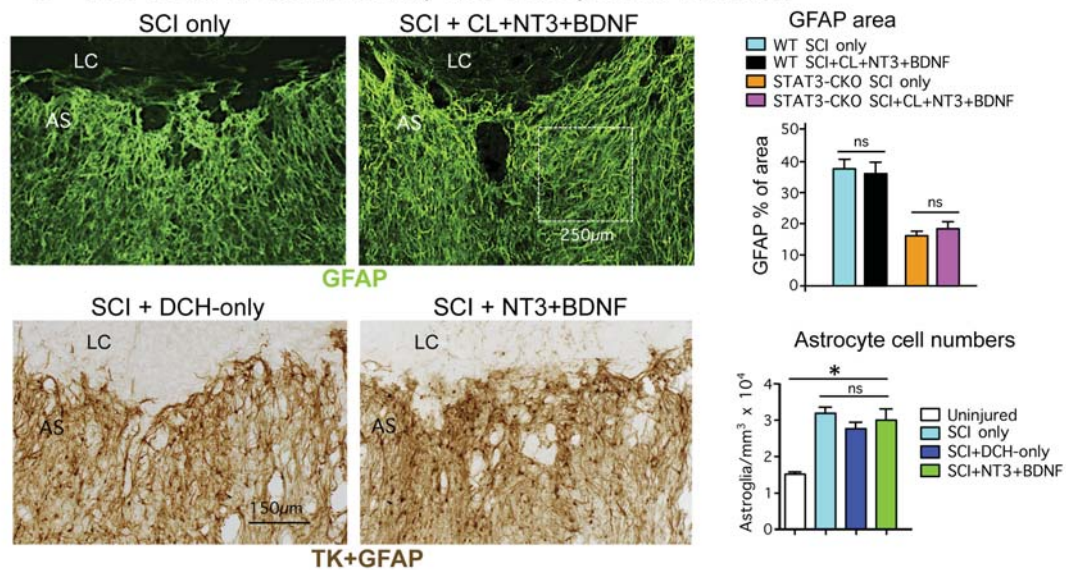
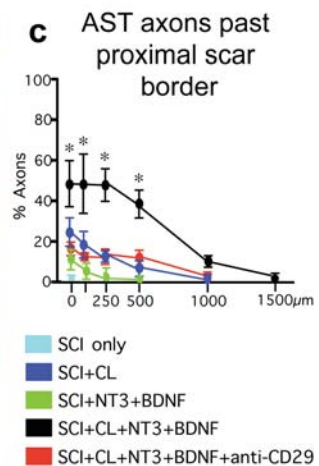
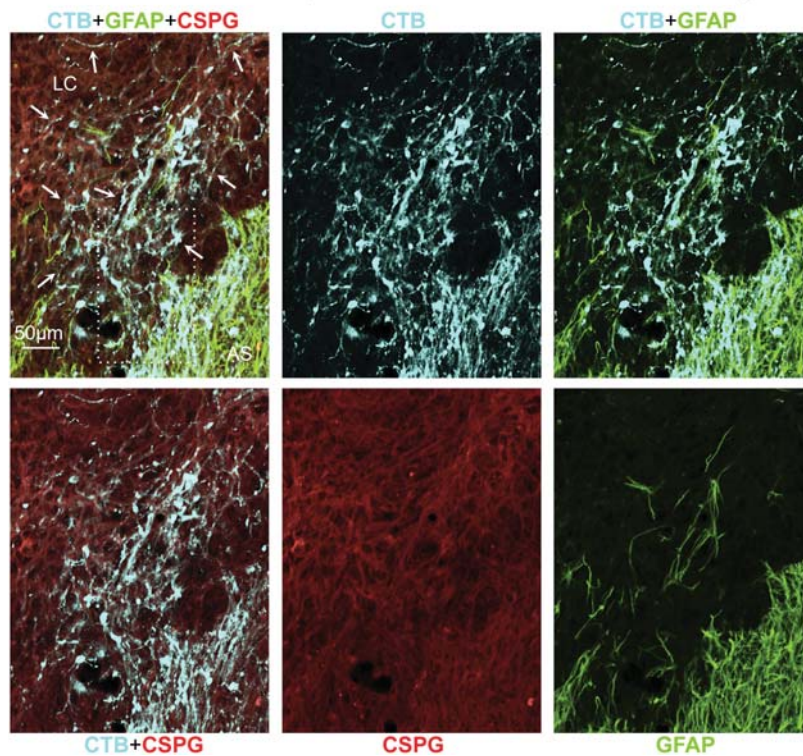




**Extended Data Figure 6 | Immunohistochemistry of specific CSPGs.**  
**a**, Neurocan (NCAN) production by scar-forming astrocytes and non-astrocyte cells. Images show individual fluorescence channels of NCAN and GFAP immunohistochemistry from horizontal sections two weeks after severe SCI, in a representative wild-type (WT) mouse. Box denotes area of lesion core (LC) and astrocytic scar (AS) shown at higher magnification. Note that NCAN is produced both by GFAP-positive scar-forming astrocytes and by non-astrocyte cells (arrows) in the lesion core. **b**, NG2 (CSPG4) production by newly proliferated scar-forming astrocytes. Images show individual channels and various combinations of immunofluorescence staining for NG2, GFAP, tdTomato (tdT), BrdU (proliferation marker) and DAPI showing astrocytes in a mature SCI scar. The images are representative of findings from tdTomato-reporter mice<sup>51</sup> injected with AAV2/5-GfaABC1D-Cre vector<sup>53</sup> into multiple sites of the uninjured spinal cord to label mature astrocytes. Three weeks after

AAV2/5-GfaABC1D-Cre injection, the mice received a severe SCI and were administered BrdU from days 2–7 after SCI. The mice were perfused after two weeks after SCI. Images comparing individual fluorescence channels show that astrocytes labelled 1 and 3: (i) incorporated BrdU and thus are newly proliferated after SCI; (ii) express the tdTomato reporter; (iii) express GFAP, the prototypical marker of reactive and scar-forming astrocytes; and (iv) express NG2 both intracellularly and along their cell surfaces. In contrast, astrocyte number 2 is also BrdU-labelled and expresses both tdTomato and GFAP, but does not appear to express detectable levels of NG2. **c**, CSPG5 (Neuroglycan C) production by scar-forming astrocytes. Images show individual channels and various combinations of immunofluorescence staining for CSPG5 or GFAP. Note that CSPG5 is present within and along the processes of GFAP-positive scar-forming astrocytes (arrows).

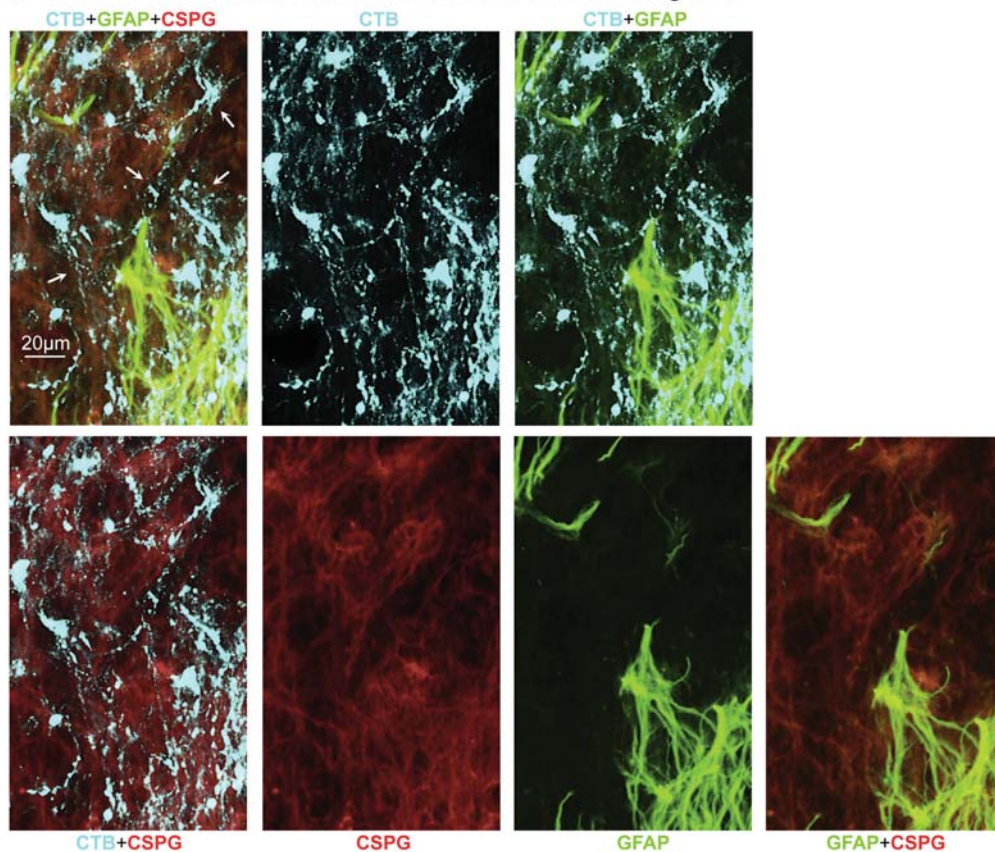
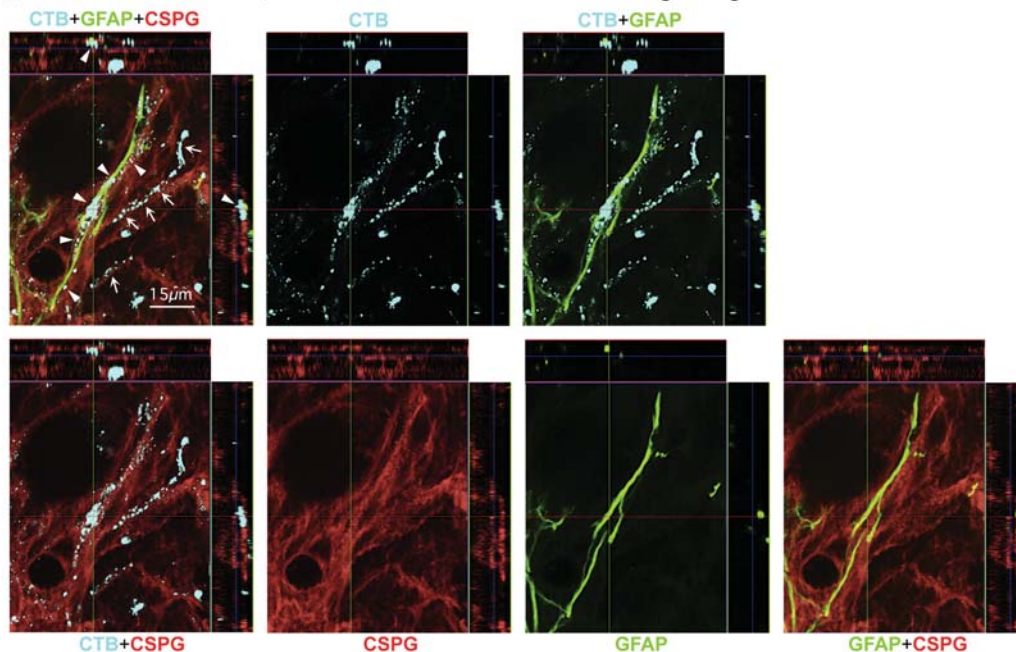


**a** NT3+BDNF do not detectably alter astrocyte scar formation**b** SCI+CL+NT3+BDNF, individual fluorescent channels of figure 5e

**Extended Data Figure 7 | Specificity and effects of treatments to stimulate AST axon regrowth after SCI.** **a**, BDNF and NT3 treatment does not alter the appearance or density of astrocyte scars in wild-type (WT) or STAT3-CKO mice. Images show horizontal sections of mice at two weeks after SCI or after SCI followed by delayed injection of hydrogel only (as a control) or hydrogel releasing NT3 and BDNF. Top images show GFAP immunofluorescence; boxed area denotes size of areas taken from multiple locations in the astrocytic scar (AS) for GFAP area quantification shown in graph.  $n = 5$  mice per group; NS,  $P > 0.05$  (ANOVA with Newman-Keuls). Bottom images show brightfield immunohistochemistry simultaneously of GFAP+TK to stain both astrocyte cell processes (GFAP) and cell bodies (TK) in mGFAP-TK transgenic mice for quantification of astrocyte cell numbers shown in graph. For these experiments the transgene-derived TK is used as a reporter protein that efficiently labels astrocyte cell bodies and thereby improves cell quantification<sup>18</sup> and the mice were not given GCV.  $n = 4$  mice per group; \* $P < 0.05$  versus

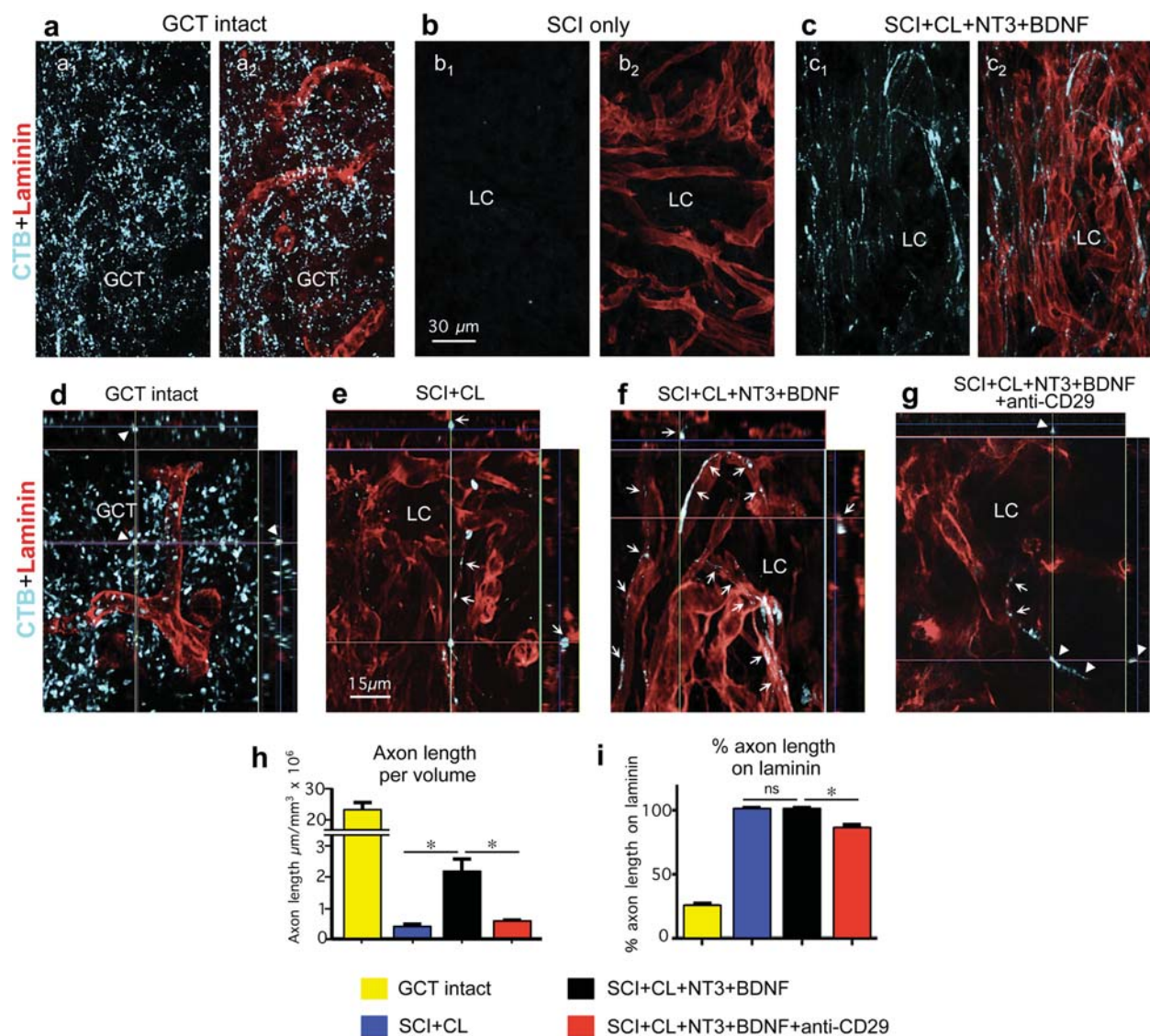
uninjured (ANOVA with Newman-Keuls); NS,  $P > 0.05$  (ANOVA with Newman-Keuls). **b**, AST axon regrowth through scar-forming astrocytes and CSPGs in SCI lesions. Images show individual channels and various combinations of immunofluorescence staining for CTB, GFAP and CS56 to detect total CSPGs from a wild-type mouse after SCI followed by delayed injection of a hydrogel depot releasing NT3 and BDNF, shown as multichannel image in Fig. 5e. Arrows denote robust regrowth of many AST axons along, through and past scar-forming astrocytes into and through the lesion core. Note that the stimulated axons are regrowing through CSPG containing areas in the astrocyte scar and lesion core. Boxed area is shown at higher magnification in Extended Data Fig. 8. **c**, Graph shows numbers of AST axons at various distances past the proximal border of the astrocytic scar under different conditions.  $n = 5$  per group; \* $P < 0.001$  significant difference SCI+CL+BDNF+NT3 versus all other groups (ANOVA with post-hoc Newman-Keuls).



**a** SCI+CL+NT3+BDNF, individual fluorescent channels of figure 5f**b** SCI+CL+NT3+BDNF, individual fluorescent channels of figure 5g

**Extended Data Figure 8 | AST axon regrowth through scar-forming astrocytes and CSPGs in SCI lesions. a, b,** Images show individual channels and various combinations of immunofluorescence staining for CTB, GFAP and CS56 to detect total CSPGs from a wild-type (WT) mouse after SCI followed by delayed injection of a hydrogel depot releasing NT3 and BDNF, shown as multichannel images in Fig. 5f, g. Arrows in **a** denote robust regrowth of many AST axons along, through and past scar-forming

astrocytes into and through the lesion core; note that the stimulated axons are regrowing through CSPG containing areas in the astrocytic scar and lesion core. **b,** High-magnification orthogonal images of axons in three visual planes. Arrows in **b** denote AST regrowing axons tracking along CSPG-positive and GFAP-negative structures. Arrowheads in **b** denote AST axons tracking along GFAP-positive and CSPG-positive astrocyte processes, passing from one astrocyte process to another.



**Extended Data Figure 9 | AST axon regrowth in SCI lesions is dependent on laminin.** **a–g**, Tract tracing of AST axons using CTB and laminin immunohistochemistry. **a–c**, Same fields imaged for CTB alone (**a**<sub>1</sub>–**c**<sub>1</sub>), or CTB plus laminin (**a**<sub>2</sub>–**c**<sub>2</sub>). **a**, **d**, Intact gracile–cuneate tract (GCT). **b**, SCI only. **c**, **f**, SCI plus conditioning lesion (CL) plus hydrogel with growth factors. **e**, SCI plus conditioning lesion. **g**, SCI plus conditioning lesion plus hydrogel with growth factors and anti-CD29. **d–g**, High-magnification orthogonal images of axons in three visual planes. Arrows indicate regrowing axons in direct contact with laminin. Arrowheads indicate axons not in direct contact with laminin in the

intact GCT (**d**) or with anti-CD29 treatment (**g**). Note the difference in appearance of axons in the intact gracile–cuneate tract (GCT), which are independent of laminin, compared with regrowing axons in lesion core (LC), which track along laminin. **h**, Axon length per tissue volume (means  $\pm$  s.e.m.) in intact GCT or in SCI lesions under different conditions. Intact GCT values were not included in ANOVA comparison of other 3 groups. **i**, Percentages (means  $\pm$  s.e.m.) of AST axon length in direct contact with laminin under different conditions.  $n = 5$  mice per group;  $*P < 0.001$  (ANOVA with post-hoc Newman–Keuls); NS, not significant (ANOVA with post-hoc Newman–Keuls).

Extended Data Table 1 | Axon growth inhibitory molecules and axon growth permissive molecules

Extended Data Table 1		Gene abbreviation	Molecule name	References for function
Axon growth inhibitory molecules		<i>Acan</i>	Aggrecan	9,29
		<i>Bcan</i>	Brevican	9,29
		<i>Ncan</i>	Neurocan	9,29,62,63
		<i>Vcan</i>	Versican	9,29
		<i>Ptprz1</i>	Phosphacan	9,63
		<i>Xylt1</i>	Xylosyltransferase 1	64
		<i>Tnr</i>	Tenascin R	65
		<i>Epha4</i>	Ephrin A4	7,66
		<i>Ephb2</i>	Ephrin B2	7,66
		<i>Efnb3</i>	Ephrin B3	7,66
		<i>Ntn1</i>	Netrin 1	7,66,67
		<i>Sema3a</i>	Semaphorin 3a	7,66
		<i>Sema3f</i>	Semaphorin 3f	7,66
		<i>Plxna1</i>	Plexin A1	7,68
		<i>Plxb1</i>	Plexin B1	7,69
		<i>Nrp1</i>	Neuropilin 1	7,70
		<i>Unc5b</i>	Netrin receptor Unc5b	7,66,71
		<i>Dcc</i>	Deleted in Colorectal Cancer	7,72,73
		<i>Neo1</i>	Neogenin 1	7,74
		<i>Rgma</i>	Repulsive guidance molecule A	7,75
		<i>Rgmb</i>	Repulsive guidance molecule B	7,75
		<i>Slit1</i>	Slit 1	7,66
		<i>Slit2</i>	Slit 2	7,66
		<i>Slitrk1</i>	SLIT and NTRK-like family, member 1	76
		<i>Robo1</i>	Robo 1	7,66
		<i>Robo2</i>	Robo 2	7,66
		<i>Robo3</i>	Robo 3	7,66
		<i>Draxin</i>	Draxin	73,77
Axon growth permissive molecule		<i>Cspg4</i>	NG2	78-81
		<i>Cspg5</i>	Neuroglycan C	82
		<i>Tnc</i>	Tenascin C	83,84
		<i>Sdc1</i>	Syndecan 1	85,86
		<i>Sdc2</i>	Syndecan 2	85,86
		<i>Sdc3</i>	Syndecan 3	85,86
		<i>Sdc4</i>	Syndecan 4	85,86
		<i>Bdnf</i>	Brain derived neurotrophic factor	35,87
		<i>Ntf3</i>	Neurotrophin 3	35,88
		<i>Gdnf</i>	Glial derived neurotrophic factor	89
		<i>Lif</i>	Leukemia inhibitory factor	90,91
		<i>Cntf</i>	Ciliary neurotrophic factor	92
		<i>Igf1</i>	Insulin-like growth factor-1	93
		<i>Fgf2</i>	Fibroblast growth factor 2	94
		<i>Tgfa</i>	Transforming growth factor alpha	95
		<i>Lama1</i>	Laminin A1	36
		<i>Lama2</i>	Laminin A2	36
		<i>Lama4</i>	Laminin A4	36
		<i>Lama5</i>	Laminin A5	36
		<i>Lamb1</i>	Laminin B1	36
		<i>Lamc1</i>	Laminin C1	36
		<i>Col4a1</i>	Collagen 4a1	8
		<i fn1<="" i=""></i>	Fibronectin 1	96
		<i>Hspg2</i>	Perlecan	86,97
		<i>Gpc1</i>	Glypican 1	86,98
		<i>Gpc3</i>	Glypican 3	86,98
		<i>Gpc5</i>	Glypican 5	86,98
		<i>Dcn</i>	Decorin	99
		<i>Lgals1</i>	Galectin 1	100
		<i>Ncam1</i>	Neural cell adhesion molecule 1	101
		<i>Matn2</i>	Matrilin	102

This table lists the gene abbreviations and full names and of the 59 axon-growth-modulating molecules whose gene expression levels are presented in Fig. 4. The table also summarizes literature providing evidence for the axon-growth-inhibitory or -permissive effects of each molecule. Refs 62–102 are cited in this table.